Charles University Prague
Faculty of Mathematics and Physics

DIPLOMA THESIS

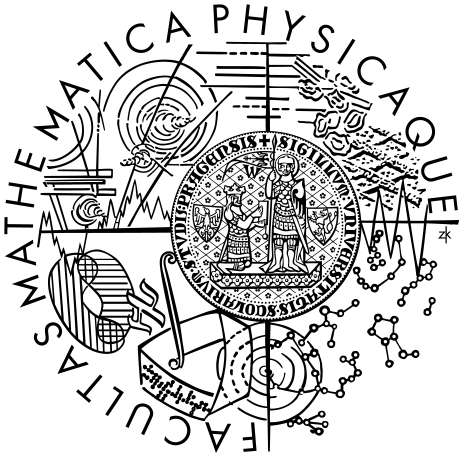

Bc. Marcela Janatová

Ultrapure metallic materials

Department of Condensed Matter Physics

Supervisor: RNDr. Jana Poltierová Vejpravová, Ph.D.

Study program: Physics, Physics of Condensed Matter and Materials

2008

Na tomto místě bych chtěla poděkovat všem, kteří se zasloužili o to, že tato diplomová práce vznikla.

Můj dík patří především RNDr. Janě Poltierové Vejpravové, Ph.D. za ochotu a trpělivost při vedení mé práce, za jazykové a odborné korektury a také za cenné rady ke zpracování a diskusi naměřených výsledků.

Dále jsem velmi vděčná Doc. RNDr. Martinu Divišovi, CSc. za výpočty hustoty stavů pro sloučeniny RCr_2Si_2C.

Děkuji také mým rodičům a bratrovi za jejich podporu během studia a Honzovi Prachařovi za pomoc při psaní v LaTeXu a za to, že mi byl v průběhu psaní této práce velkou oporou.

Prohlašuji, že jsem svou diplomovou práci napsala samostatně a výhradně s použitím citovaných pramenů. Souhlasím se zapůjčováním práce a jejím zveřejňováním.

V Praze dne 14. 4. 2008 Bc. Marcela Janatová

Contents

Název práce: Ultračisté kovové materiály
Autor: Bc. Marcela Janatová
Katedra: Katedra fyziky kondenzovaných látek
Vedoucí diplomové práce: RNDr. Jana Poltierová Vejpravová, Ph.D.
E-mail vedoucího: jana@mag.mff.cuni.cz

Abstrakt

Tato práce studuje krystalovou strukturu a magnetické vlastnosti sloučenin RCr_2Si_2 (R = Pr, Tb, Er) a RCr_2Si_2C (R = La, Ce, Pr, Nd). Všechny připravené vzorky byly charakterizovány pomocí práškové rentgenové difrakce a zkoumány pomocí měření tepelné kapacity, magnetizace a střídavé susceptibility v teplotním rozsahu 2–900 K a v magnetických polích do 9 T. U všech studovaných sloučenin výsledky ukazují na netriviální magnetické uspořádání chromové podmřížky. Dále bylo pozorováno feromagnetické uspořádání vzácnozeminné podmřížky ve sloučeninách $PrCr_2Si_2C$ a $NdCr_2Si_2C$, a také metamagnetismus v $CeCr_2Si_2C$. Pro sloučeniny RCr_2Si_2C jsme vypočítali hustotu stavů z prvních principů pomocí teorie funkcionálu hustoty. Tyto výpočty potvrzují přítomnost magnetického momentu chromu v těchto sloučeninách.

Klíčová slova: Sloučeniny RCr_2Si_2; Sloučeniny RCr_2Si_2C; Magnetické uspořádání; Tepelná kapacita; Magnetizace

Title: Ultrapure metallic materials
Author: Bc. Marcela Janatová
Department: Department of Condensed Matter Physics
Supervisor: RNDr. Jana Poltierová Vejpravová, Ph.D.
Supervisor's e-mail address: jana@mag.mff.cuni.cz

Abstract

This thesis deals with crystal structure and magnetic properties of RCr_2Si_2 (R = Pr, Tb, Er) and RCr_2Si_2C (R = La, Ce, Pr, Nd) compounds. All prepared samples were characterized by powder X-ray diffraction and investigated by specific-heat, magnetization and AC-susceptibility measurements in the temperature range 2–900 K and in magnetic fields up to 9 T. The results suggest non-trivial magnetic ordering of the Cr sublattice in all studied compounds, accompanied with ferromagnetic ordering of the Pr and Nd magnetic moments below the Curie temperature of 30 and 21 K in $PrCr_2Si_2C$ and $NdCr_2Si_2C$, respectively, and possible metamagnetism in $CeCr_2Si_2C$. For RCr_2Si_2C compounds, the experimental evidence of Cr magnetism is corroborated by results of extended first-principles calculations based on the density functional theory.

Keywords: RCr_2Si_2 compounds; RCr_2Si_2C compounds; Magnetic ordering; Heat capacity; Magnetization

Chapter 1

Introduction

The ternary intermetallic compounds of the general composition RT_2X_2 (R = rare earth, T = transition metal, X = Si or Ge) form one of the largest and intensively investigated groups of rare-earth-based ternary systems. Among them, the silicides have attracted much attention owing to the variety of physical behavior observed.

However, the RT_2Si_2 silicides containing the transition $3d$ metals larger than Mn (e.g. RCr_2Si_2 compounds) have so far rarely been investigated. Within last few years, the group of the brand new RCr_2Si_2C compounds was presented, introducing the only investigated compound – $CeCr_2Si_2C$. In fact, these compounds are the C-stabilized structure variants of the RCr_2Si_2 arrangement with light rare earths.

The crucial problem in investigation of rare earth materials is the purity of the rare-earth metals. Therefore, the goal of the thesis is employment of the solid-state electrotransport technique in order to obtain the highest available purity of the starting rare earth materials.

The aim of the thesis is to prepare novel compounds of well-defined composition and high purity, and to determine their crystal structure and magnetic properties. The key points can be summarized as follows:

- to prepare single-phase RCr_2Si_2 and RCr_2Si_2C from high-purity constituents, using rare-earth metals purified by the solid-state electrotransport,
- to characterize them by standard solid-state techniques,
- to investigate intrinsic magnetic properties of the novel compounds by various experimental techniques like magnetization and heat capacity measurements,
- to propose microscopic mechanism of magnetic ordering in the studied compounds.

The presented diploma thesis is focused on the magnetic properties of the selected RCr_2Si_2 and RCr_2Si_2C polycrystalline samples and single crystals, probed by the specific-heat, magnetization and AC-susceptibility measurements. The

characterization of the prepared compounds by means of the microprobe analysis, powder and Laue diffraction experiments is also presented. Moreover, the first-principles DFT calculations have been performed for the selected RCr_2Si_2C compounds.

This thesis is organized as following: Chapter 1 presents the aims of the diploma thesis. The theoretical background of the magnetism in metallic systems is presented in Chapter 2. Experimental techniques including the methods of syntheses, the characterization and the investigation techniques of the magnetic properties of the studied samples are described in detail in Chapter 3. Chapter 4 presents the remarks on the crystal structure and previous results of the magnetic studies of RCr_2Si_2 and RCr_2Si_2C compounds. All obtained experimental and computational results are discussed and summarized in Chapter 5. Final conclusions of the diploma thesis are presented in Chapter 6. In addition, references to the related literature are included.

Chapter 2

Theory

2.1 Magnetism in metals

2.1.1 Free electron model of metals

It is possible to understand a number of important physical properties of some metals in terms of the free electron model. In this model, the periodic potential due to the lattice is ignored. The conduction electrons in metals are delocalized and are able to move freely through the sample – they are known as the itinerant electrons.

At $T = 0$, we assume that the electrons fill states up to the Fermi wave vector k_{F}

$$k_{\mathrm{F}}^3 = 3\pi^2 n, \tag{2.1}$$

where $n = N/V$ is the number of electrons per unit volume.

The energy of the topmost filled level in the ground state (the Fermi level) is called the Fermi energy

$$\mathcal{E}_{\mathrm{F}} = \frac{\hbar^2 k_{\mathrm{F}}^2}{2m_e}, \tag{2.2}$$

where m_e is the mass of one electron.

The density of states at the Fermi level is then

$$g(\mathcal{E}_{\mathrm{F}}) = \frac{3}{2}\frac{n}{\mathcal{E}_{\mathrm{F}}} = \frac{m_e k_{\mathrm{F}}}{(\pi\hbar)^2}. \tag{2.3}$$

2.1.2 Nearly free electron model

The free electron model of metals gives us a good insight into several physical properties of metals such as the electrical conductivity and thermal conductivity, but it does not clarify, why some materials are good conductors of electricity and others are insulators or semiconductors. This is because we ignore the periodic potential due to the lattice.

However, if the periodic potential is included as a perturbation, it turns out that it has very little effect except when the wave vector of the electron is close to a reciprocal lattice vector. At such points in k-space, energy gaps appear in the dispersion relation.

Everything mentioned above was treated at $T = 0$. When $T > 0$, the density of states $g(E)$ is unchanged, but the occupancy of each state is given by the Fermi function

$$f(E) = \frac{1}{\mathrm{e}^{(E-\mu)/k_\mathrm{B}T} + 1}, \tag{2.4}$$

where μ is the chemical potential, which is temperature dependent, and k_B is the Boltzmann constant. At $T = 0$, $f(E)$ is a step function, taking the value 1 for $E < \mu$ and 0 for $E > \mu$, respectively. The step is smoothed out as the temperature increases.

The Fermi surface is the set of points in k-space whose energy is equal to the chemical potential. If the chemical potential lies in a gap, then the material is semiconductor or insulator.

2.1.3 Diamagnetism

All materials show some degree of diamagnetism, which is characterized by a weak, negative magnetic susceptibility $\chi = M/H$, where M is the magnetic moment per volume (the magnetization) and H is the applied magnetic field per unit volume. For a diamagnetic material, a magnetic field induces a magnetic moment which opposes the applied magnetic field that caused it. If we consider a solid composed of N ions (each with Z electrons of mass m_e) in volume V with all shells filled, at $T = 0$ the diamagnetic susceptibility can be expressed as

$$\chi_\mathrm{dia} = -\frac{N}{V}\frac{e^2\mu_0}{6m_e}\sum_{i=1}^{Z}\langle r_i^2\rangle, \tag{2.5}$$

where e is the charge of electron, μ_0 is the permeability of free space and r_i is the radius of the orbital of the i^th electron in the atom. Diamagnetic susceptibilities are usually largely temperature independent.

The good examples of the diamagnetic materials are ionic salts and inert noble gases.

The diamagnetic behavior comes from the diamagnetic contribution of the valence electrons, but there is also diamagnetic effect arising from the coupling of the field to the orbital motion of the conduction electrons, known as the Landau diamagnetism.

Diamagnetism is present in all materials, but it is a weak effect.

2.1.4 Paramagnetism

In practice, we measure the total susceptibility of the bulk induced by a magnetic field, which is a superposition of the Langevin diamagnetic susceptibility

(of the closed-shell ion cores), the Landau diamagnetic susceptibility, and the Pauli paramagnetic susceptibility (arising from the coupling of the intrinsic spin of the conduction electrons with the applied field H).

Paramagnetism corresponds to a positive susceptibility so that the applied magnetic field induces a magnetization, which aligns parallel with the applied magnetic field, which caused it. Here we consider the atoms, which have a nonzero magnetic moment because of unpaired electrons. Without the applied magnetic field, these magnetic moments point in random directions because the magnetic moments on neighboring atoms interact only very weakly with each other and can be assumed to be independent. The application of a magnetic field lines them up, the degree of lining up depends on the strength of the applied magnetic field.

Although an increase of magnetic field tends to line up the spins, an increase of temperature randomizes them. Therefore, the magnetization of a paramagnetic material depends on the ratio H/T. The paramagnetic effect is in general much stronger than the diamagnetic effect, although the diamagnetism is always present as a weak negative contribution.

Pauli paramagnetism

The conduction electrons also contribute to the magnetic moment of a metal. Each electron in a metal is either spin-up or spin-down. If we apply the magnetic field, the electron band is spin-split into two spin subbands. If $n_\uparrow$ is the number of electrons per unit volume with spin-up and $n_\downarrow$ is the number of electrons per unit volume with spin-down, the magnetization density is

$$M = \mu_B(n_\uparrow - n_\downarrow), \tag{2.6}$$

where μ_B is the Bohr magneton.

The Pauli paramagnetic susceptibility is given by

$$\chi_{\text{Pauli}} = \mu_B^2 g(\mathcal{E}_F). \tag{2.7}$$

As for the conduction electron magnetism, when the magnetic field H is applied, there are not only the paramagnetic effects but also the diamagnetic effects (Landau diamagnetism) as we mentioned above. For the free electrons it can be shown that

$$\chi_{\text{Landau}} = -\tfrac{1}{3}\chi_{\text{Pauli}}. \tag{2.8}$$

2.1.5 The ground state of an ion and Hund's rules

The state of an electron in a free atom or ion is described by four quantum numbers:

- n – principal quantum number
- l – orbital angular momentum quantum number

- m_l, m_s – the respective magnetic quantum numbers

A lot of electrons in the atom are found in filled shells which have no net angular momentum. However, there may be unfilled shells and the electrons in these unfilled shells can combine to give nonzero spin and orbital angular momentum. For given l there are $(2l+1)$ possible values of l_z (the z component of l): $l, l-1, l-2, \ldots, -l$ plus two values for s_z: $+\frac{1}{2}, -\frac{1}{2}$, so that the shell contains $2(2l+1)$ one-electron levels. If the electrons did not interact with each other, the ionic ground state would be $2(2l+1)$-times degenerate. However, this degeneracy is considerably lifted by electron-electron Coulomb interactions as well as by the electron spin-orbit interaction, which is the interaction of the orbital angular momentum $\mathbf{l}$ with the spin angular momentum $\mathbf{s}$ of an electron. The orbital momentum interacts more strongly with the spin moment of the same electron than with the spins of other electrons. The total angular momentum $\mathbf{j}$ of each electron is the resultant of the orbital angular momentum $\mathbf{l}$ and the spin angular momentum $\mathbf{s}$:

$$\mathbf{j} = \mathbf{l} + \mathbf{s}, \tag{2.9}$$

where the magnitude of $\mathbf{j}$ can take the values $j = l+s, l+s-1, \ldots, |l-s+1|, |l-s|$.

Hund's rules

As we can see, there are a lot of superpositions of angular momentum quantum numbers that are possible, but only one minimizes the energy and is the ground state for a particular ion. This can be estimated using Hund's rules [1]:

- The state that have the lowest energy have the largest total spin S, which is consistent with the Pauli exclusion principle.
- Among the states with the same value of S, the state with the largest total orbital angular momentum L has the lowest energy.
- Finally, with the satisfaction of the previous two rules, the value of the total angular momentum J corresponding to the state of the lowest energy is:

$$\begin{aligned} J &= |L-S| \quad \text{if the shell is less than half full,} \\ J &= L+S \quad \text{if the shell is more than half full.} \end{aligned}$$

For atoms with high atomic number Z, the spin-orbit interaction mainly dominates and the spin and orbital angular momentum of each electron is coupled separately. Then the weaker electrostatic interaction may couple the total angular momentum of each electron. This is called the j-j coupling.

After we have found the values for S, L and J, we can summarize this ground state using a term symbol ${}^{2S+1}L_J$. Here $2S+1$ is the spin multiplicity and the orbital angular momentum L is represented by one of these letters: $S, P, D, F, G, H, \ldots$ for the values of L: 0, 1, 2, 3, 4, 5, ..., respectively.

2.1.6 Crystal field

There is a pronounced difference between the rare-earth metals and transition $3d$ metals in the magnetic behavior due to the crystal field effect. In the rare-earths, the $4f$ shell (responsible for paramagnetism of the rare-earth ions) is well localized inside the ion, and is partly shielded from the environment by the outer $5s$ and $5p$ shells, respectively. In the transition $3d$ metals, $3d$ shell responsible for paramagnetism is the outermost shell in the ionic state. The $3d$ shell is thus exposed to the intense local electric field produced by the negative charged electrons in the neighboring ions. This inhomogeneous electrical field is known as the crystal field (CF).

The crystal field can be treated in the scope of the perturbation theory as follows. The total energy of the system is represented by the hamiltonian

$$\mathcal{H} = \mathcal{H}_0 + \mathcal{H}_{\mathrm{SO}} + \mathcal{H}_{\mathrm{CF}}, \tag{2.10}$$

where $\mathcal{H}_0$ is the unperturbed state, $\mathcal{H}_{\mathrm{SO}}$ is the spin-orbit coupling term, and $\mathcal{H}_{\mathrm{CF}}$ is the crystal field term.

The relation between the two perturbation terms results into the three general classes of the CF effect:

- strong CF

  $\mathcal{H}_{\mathrm{SO}} \ll \mathcal{H}_{\mathrm{CF}}$, $4d$ and $5d$ transition metal complexes

- medium-strength CF

  $\mathcal{H}_{\mathrm{SO}} \leq \mathcal{H}_{\mathrm{CF}}$, $3d$ transition metal complexes

- weak CF

  $\mathcal{H}_{\mathrm{SO}} \gg \mathcal{H}_{\mathrm{CF}}$, $4f$ intermetallic compounds

In the rare-earth ion, the spin-orbit interaction is much larger than the crystal-field interaction. Owing to this fact, it is usually sufficient to consider only the lowest multiplet J, given by Hund's rules. This limitation results in a substantial simplification both in the analysis of the experimental data and theoretical calculation. Eu^{3+} and Sm^{3+} ion states require the involvement of a higher multiplet, since the higher multiplet is just 530 and 1500 K above the ground state multiplet, respectively.

The CF Hamiltonian that describes part of the electron-electron interactions in the solid state due to the electrostatic interaction of the aspherical $4f$ charge density with the aspherical electrostatic field arising from the ion neighborhood, can be written as

$$\mathcal{H}_{\mathrm{CF}} = \sum_m \sum_n A_n^m \sum_i f_{nm}(r_i), \tag{2.11}$$

where f_{nm} are Tesseral harmonics describing the spatial distribution of the charge associated with the $4f$ electrons, A_n^m describes the spatial distribution of the charge surrounding the $4f$ electrons.

Using the Stevens formalism the summation in (2.11) over the $4f$ electrons leads to the matrix elements of the total angular momentum. Within the ground-state multiplet the crystal-field Hamiltonian (2.11) is written in the conventional form

$$\mathcal{H}_{\mathrm{CF}} = \sum_m \sum_n B_n^m \widehat{O}_n^m(J), \tag{2.12}$$

where O_n^m are the Stevens operators (equivalents) [2] and B_n^m are the crystal-field parameters which are usually evaluated from the analysis of the experimental data. The parameters B_n^m can be written as

$$B_n^m = \theta_n \langle r_{4f}^n A_n^m \rangle, \tag{2.13}$$

in which expression terms related to the $4f$ ion, θ_{4f}^n, and term related to the surrounding charges, A_n^m known as the crystal field coefficients, are separated.

For the RCr_2Si_2 and RCr_2Si_2C compounds, the local symmetry of the rare-earth ion is tetragonal, therefore the CF hamiltonian can be written as

$$\mathcal{H}_{\mathrm{CF}} = \alpha A_2^0 \langle r^2 \rangle \widehat{O}_2^0 + \beta \left(A_4^0 \langle r^4 \rangle \widehat{O}_4^0 + A_4^4 \langle r^4 \rangle \widehat{O}_4^4 \right) + \gamma \left(A_6^0 \langle r^6 \rangle \widehat{O}_6^0 + A_6^4 \langle r^6 \rangle \widehat{O}_6^4 \right), \tag{2.14}$$

where α, β, and γ correspond to the reduce matrix elements. The CF parameters can be obtained e.g. from fit of the anisotropic magnetic susceptibility.

2.2 Exchange interactions

The exchange interaction is a very important phenomenon in the theory of magnetism. Exchange interactions are responsible for magnetic ordering, in magnetic materials.

The exchange interaction is in general treated by the Heisenberg model. In the Heisenberg Hamiltonian, the exchange interaction energy between two ions is expressed by the spin Hamiltonian

$$\mathcal{H}_{ij}^{\mathrm{spin}} = -2 J_{ij} \mathbf{S}_i \cdot \mathbf{S}_j \,, \tag{2.15}$$

where J_{ij} is the exchange constant (or exchange integral) between two spins $\mathbf{S}_i$ and $\mathbf{S}_j$. Then the total spin Hamiltonian of the system, summed over all pairs of ions is

$$\mathcal{H}^{\mathrm{spin}} = -2 \sum_{\substack{i,j \\ i \neq j}} J_{ij} \mathbf{S}_i \cdot \mathbf{S}_j \,. \tag{2.16}$$

The most important simplification of the Heisenberg model is the Ising model, in which the spin $\mathbf{S}$ is replaced by his z-component, S^z. The typical example, which can be described by the Ising hamiltonian is a uniaxial system, like a tetragonal or hexagonal, with magnetic moments aligned parallel to the high-symmetry c-axis (quantization z-axis).

$$\mathcal{H}^{\mathrm{Ising}} = -2 \sum_{\substack{i,j \\ i \neq j}} J_{ij} \mathrm{S}_i^z \mathrm{S}_j^z \,. \tag{2.17}$$

There are two basic types of exchange interactions in solids: direct exchange and indirect exchange.

2.2.1 Direct exchange

The direct exchange arises from the direct Coulomb interaction among electrons, from the two neighboring magnetic atoms without the need of an intermediary (Fig. 2.1). Though this seems the most obvious route for the exchange interaction to take, the reality in physical situations is rarely that simple. The direct exchange is typical for the transition $3d$ metals such as Fe, Co and Ni.

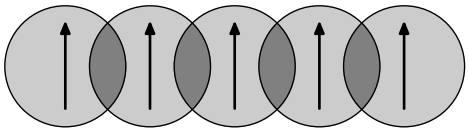

Fig. 2.1: Schematic illustration of direct exchange, in which the magnetic ions interact because their charge distributions overlap.

In rare-earths, the $4f$ electrons are strongly localized and lie very close to the nucleus, so the direct overlap between the neighboring magnetic $4f$ orbitals is negligible. This means that the direct exchange interaction is unlikely to be very effective in rare-earths. Even in transition metals, where the $3d$ orbitals extend further from the nucleus, it is extremely difficult to justify why direct exchange should lead to the observed magnetic properties.

Thus in many magnetic materials, some kind of indirect exchange interaction should be taken into the account.

2.2.2 Indirect exchange

Superexchange

In some cases, the materials have magnetic ground state, although there is no direct overlap between the orbitals of the magnetic ions. The magnetic ground state is caused by the superexchange. It can be defined as an indirect exchange interaction between the non-neighboring magnetic ions, which is mediated by atomic orbitals of a non-magnetic ion, which bridges the two magnetic ions (Fig. 2.2). The superexchange usually has an antiferromagnetic character. It is typical for ionic solids, such as MnO and MnF_2.

Indirect exchange in metals – RKKY interaction

In metals, the exchange interaction between magnetic ions can be mediated by the conduction electrons. It is known as the RKKY interaction (named after Ruderman, Kittel, Kasuya, Yosida) [4]. A localized magnetic moment spin-polarizes

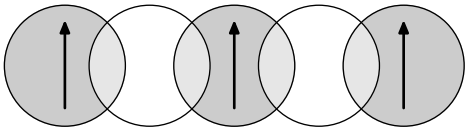

Fig. 2.2: Schematic illustration of superexchange, in which magnetic ions with non-overlapping charge distributions interact because both have overlap with the same non-magnetic ion.

the conduction electrons in its neighborhood and the spin polarization in the itinerant electrons is felt by the moments of other magnetic ions within range, leading to an indirect coupling (Fig. 2.3).

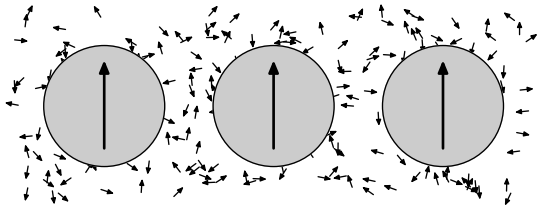

Fig. 2.3: Schematic illustration of indirect exchange, in which the interaction between magnetic ions is mediated by the conduction electrons.

The interaction is long-range and has an oscillatory dependence on the distance between the magnetic moments. Therefore, depending on the separation between two ions, the magnetic coupling may be either ferromagnetic or antiferromagnetic. This type of interaction has the basic importance in ordering of magnetic moments of well-localized electrons and is mostly found in lanthanides and their intermetallic compounds.

2.3 Types of magnetic ordering

As was mentioned above, in solids different types of magnetic interactions operate between the magnetic moments. There are several types of magnetic ground state, which can be produced by these interactions. Further, we will briefly discuss two of them – ferromagnetism and antiferromagnetism.

2.3.1 Ferromagnetism

A ferromagnet has a spontaneous magnetization – the nonzero magnetic moment even in the absence of applied magnetic field. All the magnetic moments lie along one unique direction. We define the saturation magnetization M_s as the spontaneous magnetic moment per unit volume.

To describe the ferromagnetic structures, we introduce the so-called Weiss molecular field $\mathbf{B}_{\mathrm{mf}}$, describing the interaction, which make the magnetic moments line up the same way. In fact, this molecular field measures the effect of the ordering of the system, so we can assume that $\mathbf{B}_{\mathrm{mf}}$ is proportional to the magnetization

$$\mathbf{B}_{\mathrm{mf}} = \lambda \mathbf{M}, \tag{2.18}$$

where λ is the Weiss field constant, which parametrizes the strength of the molecular field. For a ferromagnet, $\lambda > 0$. The molecular field is usually extremely large in ferromagnets due to the large Coulomb energy involved in the exchange interaction.

At low temperatures, the magnetic moments are aligned by the internal molecular field. As the temperature raises, thermal fluctuations destroy the magnetization, and at a critical temperature T_{C}, called the Curie temperature, the magnetic ordering is destroyed. This model is known as the Weiss model of ferromagnetism.

The susceptibility in ferromagnetic materials follows the Curie-Weiss law

$$\chi = \frac{C}{T - \theta_{\mathrm{p}}}, \tag{2.19}$$
$$C = \frac{N_{\mathrm{A}} \mu_{\mathrm{eff}}^2}{3 k_{\mathrm{B}}},$$

where C is the Curie constant, θ_{p} is a paramagnetic Curie temperature (which is positive in ferromagnets), N_{A} is Avogadro's number, and μ_{eff} is the effective moment. In a ferromagnet, according to the Weiss molecular field theory, $\theta_{\mathrm{p}} = T_{\mathrm{C}}$.

2.3.2 Antiferromagnetism

The antiferromagnetic state is characterized by an ordered antiparallel arrangement of the electron spins due to the fact that the dominant exchange interactions in material are negative. In the most simple case, the antiferromagnetic system is considered as two interpenetrating sublattices – in the first sublattice the magnetic moments point up, in the second point down. The nearest neighbors of each magnetic moment are those on the other sublattice. In both sublattices, there are also present the particular molecular fields at low temperatures. The molecular field disappears for temperatures above a transition temperature, known as the Néel temperature, T_{N}.

The susceptibility in antiferromagnetic materials is given in analogy with the Eq. (2.19), but a paramagnetic Curie temperature θ_{p} is negative now. In an ideal antiferromagnetic material, $\theta_{\mathrm{p}} = -T_{\mathrm{N}}$.

2.3.3 Itinerant ferromagnetism

In some materials, there is a strong evidence of the itinerant ferromagnetism in which the magnetization is caused by the spontaneously spin-split bands. Depen-

ding on the balance between the kinetic energy and the molecular field energy of electrons, the ground state of the system may be either ferromagnetic or paramagnetic. The spontaneous ferromagnetism is possible if

$$Ug(\mathcal{E}_{\mathrm{F}}) \geq 1, \tag{2.20}$$

where U is the exchange energy of electrons. This condition is known as the Stoner criterion. If the Stoner criterion is not satisfied, the spontaneous ferromagnetism will not occur and the system is paramagnetic. However, the susceptibility may be altered by the Stoner enhancement factor S_{Stoner}

$$\chi = \frac{\chi_{\mathrm{Pauli}}}{1 - Ug(\mathcal{E}_{\mathrm{F}})} = \chi_{\mathrm{Pauli}} S_{\mathrm{Stoner}}. \tag{2.21}$$

2.4 Spin-density functional theory

In real systems we cannot ignore Coulomb interactions between electrons and the effect of exchange interactions on the motion of the electrons. The positions and motions of all particles are correlated because the particles interact with each other. Thus the interactions lead to correlations appearing between particles. Such correlations can be very difficult to deal with theoretically, but a useful and successful approach is the density functional theory.

In this theory it is recognized that the ground state energy of a many-electron system can be written as a functional of the electron density $n(\mathbf{r})$. The functional contains four contributions: a kinetic energy, external-potential energy (electron-nucleus Coulomb interaction), Hartree electrostatic interaction, and a term called the exchange-correlation energy that captures all the many-body interactions beyond the Hartree term. Minimizing the energy functional leads to an equation which can be used to find the ground state energy.

The problem is that the exchange-correlation energy is unknown. However, we can use the value of the exchange-correlation energy from known results of many-electron interactions in a homogenous electron gas. This is called the local density approximation (LDA). The LDA is exact for a perfect metal (which does have uniform electron density) but is not so good for systems with wildly spatially varying electron density.

The extension of density functional theory to include the effects of spin polarization is called spin-density functional theory. In magnetic systems this is used together with the local spin-density approximation (LSDA) in which the exchange correlation potential depends not only on the local electron density but also on the local spin densities (the electron density of spin-up and spin-down electrons). This technique can be used to perform realistic calculations of electronic band structure and to obtain quantitative information concerning the spin density of real systems.

2.5 Specific heat in metallic systems

The measurement of the heat capacity of solids can provide considerable information about the lattice, electronic and magnetic properties of materials. For example, magnetic phase transitions can be seen as an anomaly in the temperature dependence of the specific heat. In solids, where the volume depends on the temperature due to the thermal expansion, we usually measure the specific heat C_p at the constant pressure

$$C_p = \left(\frac{\mathrm{d}U}{\mathrm{d}T}\right)_p \tag{2.22}$$

where U is the energy of the system.

The total specific heat of a metallic system consists of several additive contributions:

- C_e – electronic
- C_ph – lattice (phonon)
- C_mag – magnetic
- C_n – nuclear

$$C = C_\mathrm{e} + C_\mathrm{ph} + C_\mathrm{mag} \tag{2.23}$$

The nuclear part of the specific heat is related to the hyperfine interaction of the $4f$ shell with the nuclear moment of the $4f$ ion and is only significant at low temperatures for most of the $4f$ ions.

Each contribution and its origin are described in this section.

2.5.1 Electronic part

If we warm up the electrons from absolute zero to temperature T, the energy of each particle is not increased by an amount of $k_\mathrm{B}T$, but only a fraction of electrons of the order of T/T_F can be thermally excited, because only these lie within an energy range of the order of $k_\mathrm{B}T$ of the Fermi level. Then the total electronic thermal energy is

$$U \approx \frac{NT}{T_\mathrm{F}} k_\mathrm{B} T, \tag{2.24}$$

where N is the total number of electrons, and T_F is the effective Fermi temperature.

The electronic part of the specific heat is given by

$$C_\mathrm{el} = \frac{\partial U}{\partial T} \approx N k_\mathrm{B} \frac{T}{T_\mathrm{F}} \sim \gamma T. \tag{2.25}$$

The electronic contribution to the specific heat is thus proportional to T. If we express the equation (2.25) by means of the density of states at the Fermi level $g(\mathcal{E}_F)$ [3], for the specific heat of electron gas we obtain

$$C_{\mathrm{e}} = \frac{\pi^2}{3} g(\mathcal{E}_{\mathrm{F}}) k_{\mathrm{B}}^2 T. \tag{2.26}$$

2.5.2 Phonon part

At the nonzero temperature, the thermal vibrations are present in the crystal lattice. These vibrations are not independent oscillations of the individual atoms, each atom interact with its neighbors. These vibrations are treated as the travelling waves in the lattice, which are quantized in momentum and energy and are known as phonons.

The specific heat of the crystal has the following characters [1]:

- At $T = 0$, the specific heat is equal to zero.
- At the high temperatures, the value of the specific heat is approaching to the Dulong and Petit value, which is $3Nk_B$ for an ideal monoatomic crystal.
- At very low temperatures, the specific heat follows the T^3 law.

There are two theoretical models describing the behavior of the specific heat. Both models, Einstein and Debye, are discussed below.

Einstein model

The Einstein model is generally used for the approximation of the optical phonon contribution to the phonon specific heat. Within the Einstein model, we treat the thermal properties of the vibrations of a lattice of N atoms as a set of $3N$ independent harmonic oscillators in one dimension, each oscillator has the identical frequency ω_{E}. The energy U of N oscillators in the three-dimensional space is

$$U = \frac{3N\hbar\omega_{\mathrm{E}}}{\mathrm{e}^{\hbar\omega_{\mathrm{E}}/k_{\mathrm{B}}T} - 1}. \tag{2.27}$$

It is convenient to discuss results in terms of a characteristic temperature θ_{E} (called the Einstein temperature) defined by

$$\hbar\omega_{\mathrm{E}} = k_{\mathrm{B}}\theta_{\mathrm{E}}. \tag{2.28}$$

Then the specific heat is described by

$$C_{\mathrm{E}} = 3Nk_{\mathrm{B}} \left(\frac{\theta_{\mathrm{E}}}{T}\right)^2 \frac{\mathrm{e}^{\theta_{\mathrm{E}}/T}}{(\mathrm{e}^{\theta_{\mathrm{E}}/T} - 1)^2}. \tag{2.29}$$

In the high-temperature range, the C_{E} approaches the value of $3Nk_{\mathrm{B}}$, which is in the agreement with the Dulong-Petit law. However, for the low-temperature region, the specific heat drops exponentially while the experimental phonon contribution gives $C \approx T^3$.

Debye model

The Debye model of the specific heat replaces all branches of the vibrational spectrum with three branches (describing the acoustic phonons). Each branch follows the same linear dispersion relation

$$\omega = ck, \tag{2.30}$$

We can define the characteristic Debye temperature θ_{D} as

$$\hbar\omega_{\mathrm{D}} = \hbar c k_{\mathrm{D}} = k_B \theta_{\mathrm{D}}, \tag{2.31}$$

where k_{D} is the maximum inverse interparticle spacing, and ω_{D} is the maximum phonon frequency. Then we can write the formula for the specific heat

$$C_{\mathrm{D}} = 9Nk_{\mathrm{B}} \left(\frac{T}{\theta_{\mathrm{D}}}\right)^3 \int_0^{\theta_{\mathrm{D}}/T} \frac{x^4 \mathrm{e}^x dx}{(\mathrm{e}^x - 1)^2}. \tag{2.32}$$

In the high-temperature region, the specific heat C_{D} follows the Dulong-Petit law. Moreover, at low temperatures the specific heat follows the T^3 law, which is in the agreement with experiments. That's why the Debye theory is widely used for explanation of the specific heat of the crystal lattice.

Anharmonicity

Behavior of a real crystal lattice does not completely correspond to the theoretical models. All the phonon contributions to the specific heat were treated within the harmonic approximation, in which we assume that there is no thermal expansion. However, this condition is not satisfied in real crystals, the anharmonic terms must be taken into the account.

In solid, there are two types of phonon branches: low-energy acoustic phonons and optical phonons as the vibrational states populated in higher energy levels. Debye model describes the acoustic phonon branches ($3\times$ degenerated) while the Einstein model is useful to characterize the optical phonons ($3n-3$ modes, n is the number of atoms per unit cell). As both models postulate the harmonic oscillators, they do not consider thermal expansion and thus describe the isochoric specific heat. In reality, the volume changes with temperature and we measure the isobaric specific heat C_p. Therefore, the anharmonicity corrections must be involved [5].

The total specific heat is then expressed as

$$C_{\mathrm{ph}} = R \left(\frac{1}{1 - \alpha_{\mathrm{D}} T} C_{\mathrm{D}} + \sum_{i=1}^{3n-3} \frac{1}{1 - \alpha_{\mathrm{E}i} T} C_{\mathrm{E}i} \right), \tag{2.33}$$

where R is the universal gas constant, and α_{D} and α_{E} is the anharmonic term for acoustic and optical phonon branches, respectively.

2.5.3 Magnetic part

In $4f$ compounds, a magnetic contribution to the specific heat is associated with increasing population of the excited localized states. The degeneracy of the $4f$ ground state multiplet is lifted by the crystal-field effect and molecular-field interactions. The splitting of the $(2J+1)$-fold degeneracy of the ground-state multiplet due to the crystal field follows the well-known Kramer's theorem.

However, it is difficult in general to separate the magnetic part from the other contributions. The so-called nonmagnetic analogues (isostructural compounds with nonmagnetic rare-earth ion) are therefore taken as a reference for the nonmagnetic part of the specific heat, in order to obtain the magnetic contribution to the C_{p}.

In the paramagnetic state, the magnetic part of the specific heat is given by the Schottky-type contribution only. Then the crystal-field level scheme can be obtained from the analysis of the specific heat in the paramagnetic state.

When we separate the crystal-field part of the specific heat, a contribution due to the magnetic ordering is finally obtained.

Chapter 3

Experimental

3.1 Sample preparation

3.1.1 Polycrystalline samples – mono-arc furnace

The polycrystalline samples were synthesized in the mono-arc furnace installed in the Technology Laboratory of the Department of Condensed Matter Physics (DCMP), Charles University. The samples were four times re-melted to improve homogeneity. Prior to the sample preparation, the constituent rare-earth elements had been refined by solid-state electrotransport (SSE).

The mono-arc apparatus consists of the sample chamber, torch, vacuum system, water-cooling system and power supply for the arc. First, the constituent elements are set in the water-cooled copper crucible inside the apparatus. Then the sample chamber must be evacuated for at least 1 hour and after that the chamber is filled with the protective argon atmosphere.

For the syntheses, we used the constituent elements of the following purities: R of 4N, Cr of 4N6, Si of 5N and C of 3N. Each sample was carefully melted for about 1 minute, initial stoichiometries are presented in Table 3.1.

Compound	R	m_{R} (g)	m_{Cr} (g)	m_{Si} (g)	m_{C} (g)	Final mass (g)
$PrCr_2Si_2$	Pr	0.8552	0.6314	0.3411		1.8277
$TbCr_2Si_2$	Tb	0.9774	0.6394	0.3454		1.9622
$ErCr_2Si_2$	Er	1.0717	0.6664	0.3599		2.0978
$LaCr_2Si_2C$	La	0.9028	0.6757	0.3652	0.0780	2.0217
$CeCr_2Si_2C$	Ce	1.0371	0.7695	0.4160	0.0890	2.3116
$PrCr_2Si_2C$	Pr	0.9093	0.6710	0.3627	0.0773	2.0203
$NdCr_2Si_2C$	Nd	0.9588	0.6912	0.3733	0.0798	2.1031

Table 3.1: The initial stoichiometries and constituent elements for syntheses of RCr_2Si_2 and RCr_2Si_2C compounds.

3.1.2 Single crystals – tri-arc furnace

The single crystals of $CeCr_2Si_2C$ and $PrCr_2Si_2C$ composition were grown from about 6 g of melt in the tri-arc furnace at the Department of Condensed Matter Physics. The apparatus utilizes the Czochralski pulling technique modified for arc heating and consists of the sample chamber, vacuum system, water-cooling system, power supplies for the three arcs, and the pulling head with continuously controllable rotation and translation.

After the sample is set inside the apparatus, the sample chamber is evacuated for approximately half a day, and subsequently filled with the protective argon atmosphere. The melt is then heated with three symmetrically-positioned arcs while the copper crucible is rotating and water-cooled.

We used the tungsten rod (instead of a polycrystalline seed), which was dipped into the melt in the rotating crucible, and then slowly and carefully pulled upwards with the typical pulling speed 8–10 mm/hour. The random necking procedure was performed to form the ingot. The pulling ingot is tapered into the thin neck, where only a single crystalline grain is propagated. Then the ingot is slowly broadened. When the satisfactory piece of material has been grown, proper tapering of the sample separates the crystal from the melt.

3.1.3 Solid-state electrotransport

Introduction

When an electric field is applied to a metal, in addition to the flow of electrons, a small transport of matter also occurs. This process of mass transport is referred to as electrodiffusion, electromigration or electrotransport. In the solid state, it is manifested in (a) self-transport in pure metals arising from the displacement of atoms into vacancies, (b) the separation of the components of a substitutional alloy resulting from their different rates or directions of migration, and (c) the transport of interstitial solutes.

Purification of metals by solid state electrotransport

One application of the electrotransport phenomenon is in the preparation of pure metals and high-quality metallic crystals. However, the electrotransport process is very inefficient, and so, in terms of purification per unit of energy consumed, any technique based on electrotransport would appear to be of limited value. Nevertheless, techniques have been developed which provide small quantities of high-purity metals, superior to that produced by alternative methods. Such materials are highly desirable in experimental solid state research, where the high purity is a pre-requisite. The purification technique, often referred to as solid state electrotransport (SSE) processing [6], has certain advantages, particularly for reducing the concentration of interstitial impurities.

Principle of SSE processing

During the SSE process, a metallic rod containing initially a dilute uniform concentration, C_i^0, of a solute i is subjected to a direct current. The rod is heated and we assume that it attains a constant temperature throughout its length. Furthermore, there is no solute flux through the ends or surface of the rod. The equation for the solute migration flux J_i in the x direction is

$$J_i = -U_i C_i E - D_i \frac{\mathrm{d}C_i}{\mathrm{d}x}, \tag{3.1}$$

where C_i is the actual concentration of the solute i, U_i is the mobility of the solute i and E is the electrical field intensity. After a sufficiently long time, the concentration at any point is time-independent (J_i) and a steady state is reached. The electrotransport flux (towards the anode) balances the back diffusion flux (towards the cathode). The concentration decays exponentially:

$$C(x, \infty) = K \exp\left(\frac{-UEx}{D}\right). \tag{3.2}$$

For interstitial solutes (and very short rod), the migration constant K is given by

$$K = \frac{C_0 UEl}{D}, \tag{3.3}$$

where l is the rod length.

SSE apparatus

All rare-earth metals used for preparation of the studied samples were purified using the SSE apparatus installed in the DCMP. The SSE apparatus consists of the following compartments:

- Working chamber

  The working chamber is equipped with a chamber-baking system. The baking procedure allows degassing of the chamber from residual gases and possible contaminants.

- Pumping system

  The necessary high vacuum in order of 10^{-10} Pa and better in the chamber during the process is reached by the 4-step pumping system.

- Sample maintaining – fabricated from copper

- Cooling system

- Sample-temperature control

3.2 Sample characterization

3.2.1 X-ray powder diffraction

All prepared samples were characterized by powder X-ray diffraction (XRD) with Seifert XRD 7 diffractometer at DCMP working with the Bragg-Bretano geometry. The XRD patterns were recorded at room temperature using Cu K_α radiation. The 2Θ scans were performed within 20°–100° range by a 0.04° step with the 5 second exposition per point. All the XRD data were analyzed by the Rietveld technique [7] using the program FULLPROF for refinement of the crystal structure.

3.2.2 Laue method

The standard Laue method (in the reflection configuration [9]) has been used both to determine the single-crystallinity of the grown ingot, and to orient the sample for further experiments. Laue patterns were taken on Mikrometa apparatus with Cu radiation. Goniometric head was used to fix a proper orientation of an ingot. After reaching the required orientation of the sample, the single crystal was carefully cut for further experiments using a spark cutter.

3.2.3 Scanning electron microscopy

Homogeneity and stoichiometry of the $LaCr_2Si_2C$, $CeCr_2Si_2C$ and $PrCr_2Si_2C$ compounds were investigated by field-emission high resolution scanning electron microscopy (SEM) with MIRA II LMU (TESCAN). The device is equipped with SE (secondary electrons) and BSE (back-scattered electrons) detectors. The accelerating voltage is in the range 200 V–30 kV, and at 30 kV, the resolution is 1 nm and 2 nm for SE and BSE detector, respectively.

All three compounds were investigated by EDAX (Energy Dispersive X-ray analysis), which is the technique used for identifying the stoichiometric composition of the studied sample.

3.3 Magnetization measurements

Magnetization measurements were performed using two instruments, installed at the Joint Laboratory for Magnetic Studies: PPMS (Physical Property Measurement System) [10] and MPMS (Magnetic Property Measurement System) – SQUID magnetometer [11], both from Quantum Design.

3.3.1 PPMS

In the PPMS facility, there are two basic options used for magnetic measurements – ACMS and VSM. Both options are discussed in this section.

ACMS

All polycrystalline samples were investigated using the standard AC Measurement System (ACMS) option in the temperature range 2–350 K and magnetic fields up to 9 T. Data have been recorded on fine-powder samples with randomly oriented grains, fixed by diluted glue in a small gelatine capsule. The mass of those samples was approximately 40–190 mg, adjusted according to the measured signal.

The ACMS option enables to measure both the magnetization and the AC susceptibility. The distinction between the two types of measurements is important. During DC measurements, a constant field is applied to the measurement region and the sample is moved quickly through the detection coils, inducing a signal in them according to Faraday's law. This method measures a sample's magnetic moment M in an applied magnetic field H at a specific temperature T ($M = M(H, T)$). During AC measurements, an alternating field is applied to the measurement region and the sample is positioned in the center of each detection coil. The detection coils indicate, how the applied field is altered by the presence of the sample. This method do not directly measure a sample's magnetic moment, but it is very useful for examining the nature of magnetic phase transitions, such as ferromagnetic transitions. Typically, a magnetic susceptibility diverges at the critical temperature of a ferromagnetic phase transition.

In the ACMS option, AC measurements are nearly three orders of magnitude more sensitive than DC measurements – within the AC susceptibility measurement, the samples with the magnetic moment in order of $\sim 10^{-5}\,\mathrm{Am}^2$ can be detected, while the DC measurement system can detected the moment in order $\sim 10^{-2}\,\mathrm{Am}^2$.

The AC-susceptibility data for polycrystalline samples were collected in the temperature range 2–40 K at the frequency $f = 1\,\mathrm{kHz}$ with the amplitude of the AC-magnetic field $A = 1\,\mathrm{mT}$.

VSM

All single crystals were investigated using the VSM (Vibrating Sample Magnetometer) option. The high-temperature DC magnetization measurements were performed using the VSM Oven option for all studied samples. During the measurement, the sample holder with a sample oscillates near a detection coil, a changing magnetic flux induces a voltage in the detection coil and this voltage is synchronously detected.

The samples were investigated as small bulk pieces (the samples mass was 3–10 mg). Within the VSM option, the sample is mounted on the special paddle-shaped sample holder using the glue and inserted into the sample chamber. Then we can perform the magnetization measurement in the temperature range 2–350 K. As for the VSM Oven option, the data can be collected in the temperature range 300–900 K. For this kind of measurement, the special VSM Oven

heater stick is required. This heater stick is a device that contains platinum resistor heater, thermometer, and a sample holder for the oven option. The sample is mounted on the sample holder using alumina cement. Then the sample holder is wrapped with a thin copper foil, which reduces thermal gradients between the sample and heater stick. Heating of the sample is achieved by applying current to the platinum resistor heater. A thermocouple embedded on the back side of the sample holder measures the temperature in the sample region, and a thermistor at the top connector of the sample holder corrects for heating of the cold junction.

The PPMS VSM option performs sensitive measurement - the system is able to resolve magnetization changes of less than $\sim 10^{-3}\,\mathrm{Am}^2$.

3.3.2 SQUID magnetometer

Some additional measurements of DC magnetization and AC susceptibility for RCr_2Si_2C compounds were performed with a MPMS facility which uses a SQUID (superconducting quantum intereference device) and therefore it enables to perform one of the most sensitive magnetization measurement. SQUID is a superconducting ring with a Josephson junction in it, and the ring is able to act like a very sensitive quantum interferometer. If a sample is passed through the ring, the induced persistent current is proportional to the magnetization of the sample. In this case, it is possible to detect the magnetic moments in the order of $\sim 10^{-12}\,\mathrm{Am}^2$.

For this measurement, the polycrystalline samples were used in the same form as for ACMS measurement. Single crystal of $PrCr_2Si_2C$ was measured in the form of a bulk piece with the orientation of the magnetic field along the (001) and (100) crystallographic direction.

In the case of $PrCr_2Si_2C$ single crystal, we measured AC susceptibility in the temperature range 15–45 K at frequencies 1 Hz, 10 Hz, 100 Hz and 1 kHz with the amplitude $A = 0.3\,\mathrm{mT}$.

3.4 Specific heat measurements

The specific heat measurement was performed with a PPMS (Quantum Design) facility.

The samples were mounted on the Al_2O_3 platform ($3\,\mathrm{mm} \times 3\,\mathrm{mm}$) using a thin layer of Apiezon N Grease, which provides the required thermal contact to the platform. A platform heater and platform thermometer are attached to the bottom side of the sample platform. Small wires provide the electrical connection to the platform heater and platform thermometer.

The pressure within the probe must be less than approximately 1 mTorr, so that the thermal conductance between the sample platform and the thermal bath (puck) is totally dominated by the conductance of the wires.

During a measurement, a known amount of heat is applied at constant power for a fixed time, and then this heating period is followed by a cooling period of the same duration. After each measurement cycle – which is a heating period followed by a cooling period – data are fit in the entire temperature response of the sample platform to the two tau model, which is used when poor thermal attachment of the sample to the platform produces a temperature difference between the two.

All polycrystalline samples were investigated by the specific heat measurement. The single crystal of $PrCr_2Si_2C$ was measured in several magnetic fields applied parallel to the (001) crystallographic direction.

The typical mass of the samples was about 5–10 mg. Flat thin samples with the smooth surface were chosen for the measurement because of the best achievable thermal contact with the platform.

3.5 First-principles calculations

To obtain direct information about the ground-state electronic structure and magnetic properties of $LaCr_2Si_2C$ and $PrCr_2Si_2C$, we have applied first-principles theoretical methods. The ground-state electronic structure was calculated on the basis of the density functional theory (DFT) within the local spin density approximation (LSDA) [12] and generalized gradient approximation (GGA) [13]. For this purpose, we used the full-potential augmented plane wave plus local orbital method (APW + lo) as implemented in the latest version (WIEN2k) of the original WIEN code [14]. The calculations were scalar relativistic and were performed with the following parameters. Non-overlapping atomic-sphere radii of 2.8, 2.3, 1.6 and 1.2 a.u. (1 a.u. = 52.9177 pm) were taken for R, Cr, Si and C, respectively. The basis for expansion of the valence states (less than 8 Ry below the Fermi energy) consisted of more than 800 basis functions (more than 100 APW/atom) plus R ($5s$, $5p$), Cr ($3s$, $3p$), Si ($2p$) and C ($2s$) local orbitals. The Pr $4f$ states are localized and were treated in the open-core approximation with the stable atomic configuration $4f^2$. The Brillouin-zone (BZ) integrations were performed with the tetrahedron method [14] on a 168 special k-point mesh (2000 k-points in the full BZ). We carefully tested the convergence of the results presented with respect to the parameters mentioned and found them to be fully sufficient for all presented characteristics of RCr_2Si_2C compounds.

Chapter 4

RCr_2Si_2 and RCr_2Si_2C compounds – Previous results

4.1 Crystal structure

RCr_2Si_2 compounds

The RT_2X_2 compounds usually crystallize in the $ThCr_2Si_2$-type body-centered tetragonal structure. The $ThCr_2Si_2$ structure type, in which also some of the RCr_2Si_2 compounds crystallize, has the space group $I4/mmm$ with the standardized atom coordinates:

- R at $2a$: 0, 0, 0
- Cr at $4d$: 0, 1/2, 1/4
- Si at $4e$: 0, 0, z

RCr_2Si_2	a(Å)	c(Å)	c/a	z
$SmCr_2Si_2$	3.9650	10.700	2.699	
$GdCr_2Si_2$	3.9408	10.663	2.706	0.379
$TbCr_2Si_2$	3.9231	10.651	2.715	0.381
$DyCr_2Si_2$	3.9073	10.632	2.721	
$HoCr_2Si_2$	3.8990	10.625	2.725	0.377
$ErCr_2Si_2$	3.8885	10.614	2.730	
$TmCr_2Si_2$	3.8774	10.605	2.735	
$YbCr_2Si_2$	3.8677	10.603	2.741	
$LuCr_2Si_2$	3.8626	10.586	2.741	

Table 4.1: Crystallographic data for the RCr_2Si_2 compounds according to [15].

The atoms are stacked along the c-axis in layers in the sequence R-X-T-X-R-X-T-X-R... (Fig. 4.1). The unit cell contains two formula units of RCr_2Si_2.

The table 4.1 shows the summary of lattice parameters of the RCr_2Si_2 compounds according to [15].

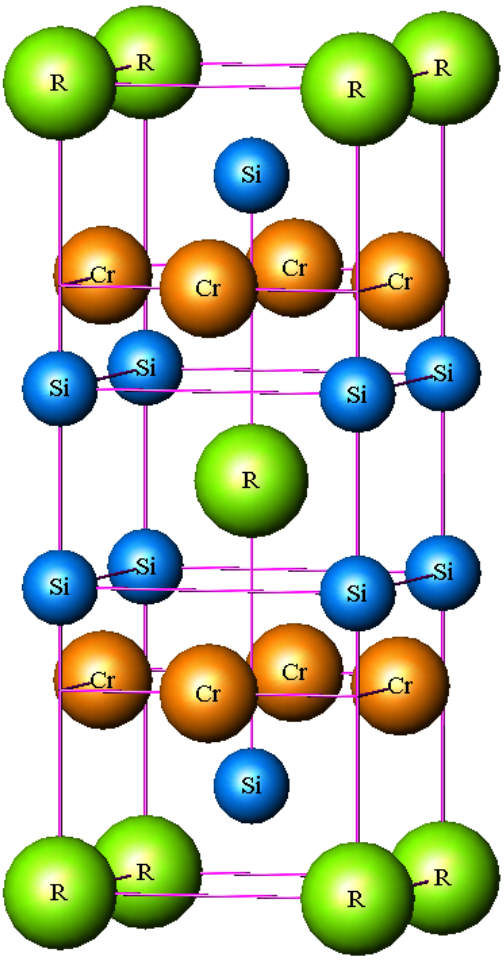

Fig. 4.1: Crystal structure of RCr_2Si_2 compounds.

RCr_2Si_2C compounds

It has been reported that the $ThCr_2Si_2$-type structure is stable only for the rare-earth ions from Sm to Lu in RCr_2Si_2 compounds [15–18]. The RCr_2Si_2 compounds with the light rare-earth ion do not form a stable phase. Instead, a structure variant can be stabilized by inserting one carbon atom per formula unit. The crystal structure can be described as $CeMg_2Si_2$-based tetragonal type (Fig. 4.2), which is another primitive variant of the $ThCr_2Si_2$-type structure. The atoms occupy the following positions of the space group $P4/mmm$:

- 1R at 1*a*: 0, 0, 0
- 2Cr at 2*e*: 0, 1/2, 1/2
- 2Si at 2*h*: 1/2, 1/2, *z*
- 1C at 1*b*: 0, 0, 1/2

The unit cell contains only one formula unit of RCr_2Si_2C.

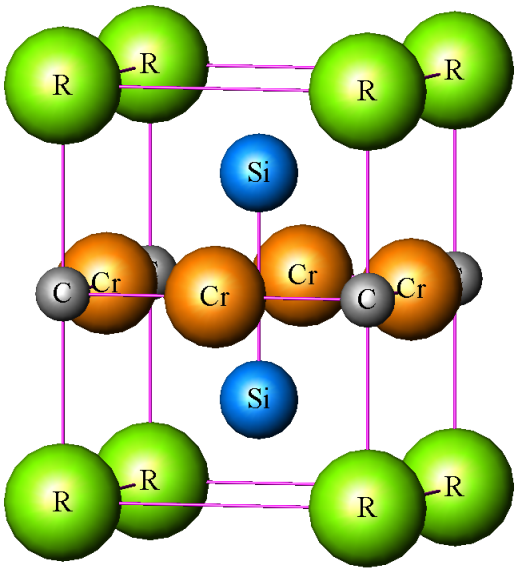

Fig. 4.2: Crystal structure of RCr_2Si_2C compounds.

4.2 Magnetic properties

RCr_2Si_2

In the RT_2Si_2 compounds, the transition-metal sublattice exhibits magnetic ordering in some cases [19]. For example, numerous neutron diffraction investigations of the RMn_2Si_2-type compounds have proved that the Mn sublattice orders antiferromagnetically below 500 K, whereas the rare-earth magnetic moments exhibit ordering at much lower temperatures [20]. In contrast, in the RT_2Si_2 compounds with T = Fe, Ni, Co and the corresponding 4*d* and 5*d* analogues, the transition metal subsystem can be classified as a Pauli paramagnet, and only the rare-earth sublattice orders magnetically [21]. The only reliable report of stable Cr magnetic moments larger than $1.5\mu_B$, ordered at least up to 470 K, was given for $HoCr_2Si_2$ by Moze et al. [22].

In the following section, the up to date published results of the investigation of RCr_2Si_2 and RCr_2Si_2C compounds, respectively, are listed. We would like to point out, that the available reports are rare and rather inconsistent.

$TbCr_2Si_2$

$TbCr_2Si_2$ orders antiferromagnetically below $T_N = 2.4\,K$ as presented by Dommann et al. [15]. On the basis of the results of magnetic susceptibility measurement, Dommann et al. obtained the values for an effective magnetic moment $\mu_{eff} = 9.4\mu_B$ and a paramagnetic Curie temperature $\theta_p = -37\,K$.

In contrast to [15], Moze et al. [18] presented the paramagnetic Curie temperature of this compound as $\theta_p = -2.6\,K$. Moreover, they claimed, that the Cr sublattice orders antiferromagnetically with Néel temperature $T_N = 758\,K$ obtained from the differential scanning calorimetry. No long range magnetic order of the Tb sublattice in $TbCr_2Si_2$ is observed by authors of [18].

$ErCr_2Si_2$

In $ErCr_2Si_2$, the Er sublattice orders ferromagnetically below 2.4 K as revealed the neutron diffraction experiment performed by Moze et al. [18]. Moreover, no short range ordering at low temperatures in $ErCr_2Si_2$ was observed by the authors of [18].

Moze et al. also presented that the Cr sublattice orders antiferromagnetically with Néel temperature $T_N = 692\,K$, which was observed by the differential scanning calorimetry.

RCr_2Si_2C

The only report on the RCr_2Si_2C compounds was given by Tang et al. [23]. They claimed that the $CeCr_2Si_2$ does not exist, probably due to the large atomic radius of Ce. Instead, they investigated the structure variant – $CeCr_2Si_2C$.

$CeCr_2Si_2C$

The $CeCr_2Si_2C$ compound was investigated only by the magnetic susceptibility measurement in the temperature range 300–600 K [23]. The inverse susceptibility follows a Curie-Weiss law with an effective magnetic moment of $\mu_{eff} = 2.83\mu_B$, and a paramagnetic Curie temperature of $\theta_p = -299\,K$. The μ_{eff} value is not far off from the free ion value of Ce^{3+} ($2.54\mu_B$). Probably, the Ce is in the Ce^{3+} ionic state in this temperature range. However, Tang et al. claimed, that the abnormally large negative θ_p value could be rather indicative of a mixed-valence state of Ce.

Chapter 5

Results and discussion

5.1 Sample preparation

For our investigations, we have prepared the polycrystalline samples of the following compositions (see Table 3.1): $PrCr_2Si_2$, $TbCr_2Si_2$, $ErCr_2Si_2$, $LaCr_2Si_2C$, $CeCr_2Si_2C$, $PrCr_2Si_2C$ and $NdCr_2Si_2C$. All studied samples were melted successfully, only the $PrCr_2Si_2$ composition was extremely reluctant to melting, and finally resulted in a hard multi-phase material. All RCr_2Si_2C compounds showed a good tendency to crystallize (Figs. 5.1 and 5.2), so we decided to prepare also single crystals.

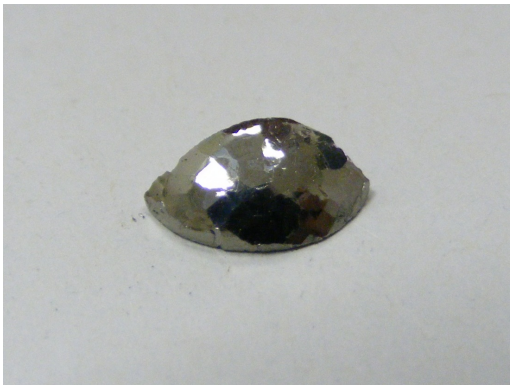

Fig. 5.1: Polycrystalline sample of $LaCr_2Si_2C$.

Fig. 5.2: Polycrystalline sample of $CeCr_2Si_2C$.

In sequence, we tried to synthesize three single crystals using the Czochralski method: $LaCr_2Si_2C$, $CeCr_2Si_2C$ and $PrCr_2Si_2C$.

We made three attempts to prepare $LaCr_2Si_2C$ single crystal, but the melt-ingot system became unstable, the melt was overcooled and the final ingot was found to be polycrystalline. We were more successful with preparation of the $CeCr_2Si_2C$ and $PrCr_2Si_2C$ single crystals, although we had similar problems with the overcooling of the melt as with the La compound.

5.2 Sample characterization

5.2.1 Powder X-ray diffraction

All prepared samples were characterized by powder XRD and found to be single-phased except the $PrCr_2Si_2$ compound. The XRD patterns were reliably described by the proposed crystal structures in all cases. As an example, the observed and calculated diffraction patterns of $TbCr_2Si_2$ and $LaCr_2Si_2C$ are displayed in Figs. 5.3 and 5.4, respectively.

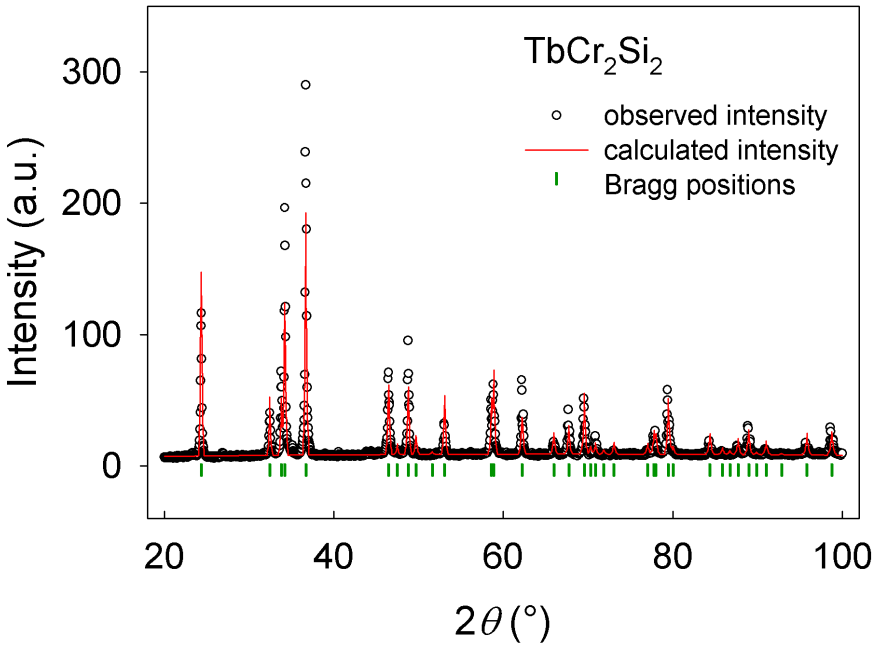

Fig. 5.3: Observed and calculated diffraction pattern of $TbCr_2Si_2$. Tick marks indicate the calculated Bragg positions.

As we mentioned above, we were unsuccessful to synthesize the $PrCr_2Si_2$ compound. The powder XRD confirmed the multi-phase composition of the compound. The diffraction pattern of this material is displayed in Fig. 5.5. As we can see, there are a lot of peaks not belonging to $PrCr_2Si_2$ phase. After the XRD experiment, we decided to stop further investigations of this sample.

As we can see, there is rather poor agreement between the observed and calculated powder XRD intensities for RCr_2Si_2C. The main discrepancy occurs for the (002), (102) and (004) diffraction peaks. This suggests that the samples possess a strong preferential orientation along the c-axis. Probably, this is due to the fact that the samples were measured as-cast and additional heat treatment may decrease the observed effect in the material.

The lattice parameters and the z parameters of the Si atoms of RCr_2Si_2 and RCr_2Si_2C compounds obtained on the basis of the Rietveld analysis are listed

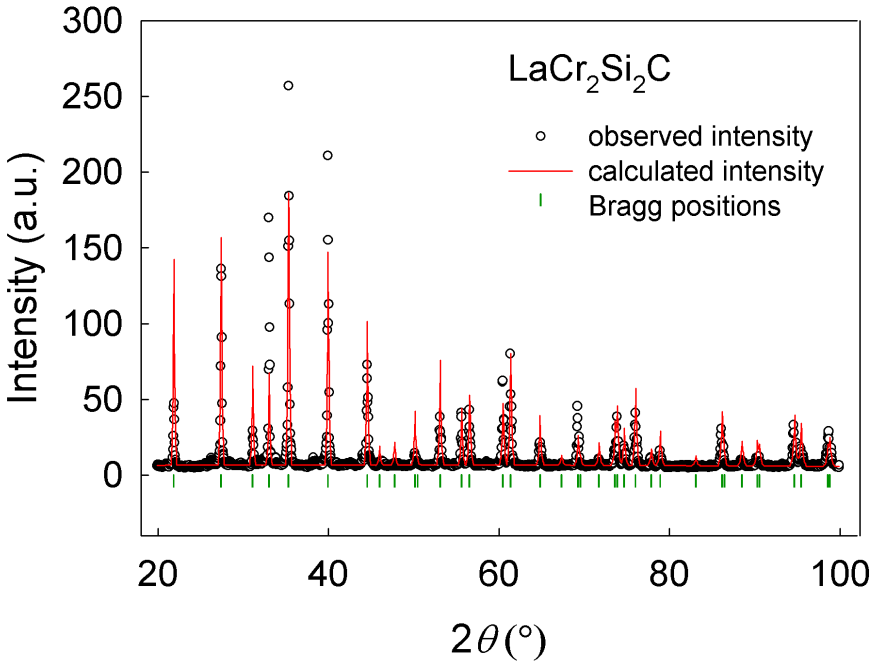

Fig. 5.4: Observed and calculated diffraction pattern of $LaCr_2Si_2C$. Tick marks indicate the calculated Bragg positions.

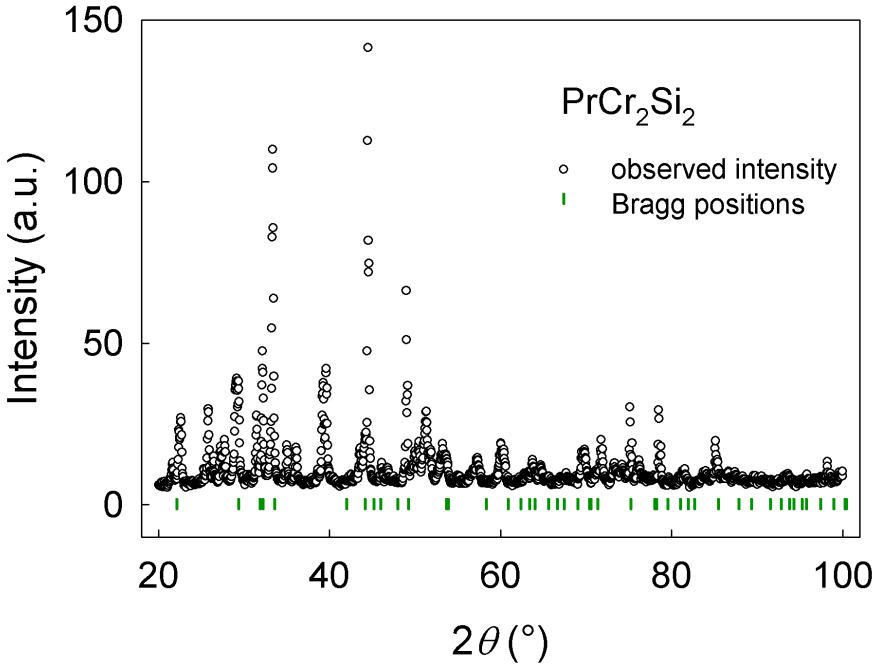

Fig. 5.5: Observed diffraction pattern of $PrCr_2Si_2$. Tick marks indicate the calculated Bragg positions.

in Table 5.1.

Compound	a(Å)	c(Å)	c/a	V(Å^3)	z
$TbCr_2Si_2$	3.919	10.647	2.717	163.495	0.390
$ErCr_2Si_2$	3.888	10.621	2.732	160.537	0.391
$LaCr_2Si_2C$	4.065	5.420	1.333	89.539	0.231
$CeCr_2Si_2C$	4.013	5.278	1.315	85.020	0.228
$PrCr_2Si_2C$	4.022	5.340	1.328	86.389	0.228
$NdCr_2Si_2C$	4.018	5.333	1.327	86.097	0.232

Table 5.1: Crystallographic data for RCr_2Si_2 and RCr_2Si_2C obtained by Rietveld analysis at room temperature.

The calculated lattice parameters for RCr_2Si_2 are in good agreement with the pronounced values according to [15]. In the case of RCr_2Si_2C compounds, the lattice parameters decrease with the increasing atomic number of the rare earth, which is expected behavior due to the lanthanide contraction. The only exception is the $CeCr_2Si_2C$ compound – the lattice parameters are smaller than those of the Pr compound. This effect may be caused by the fact that the ionic state of Ce is Ce^{4+} rather than Ce^{3+}.

5.2.2 Laue method

The Laue patterns were taken to examine the single-crystallinity of the grown ingots of the $LaCr_2Si_2C$, $CeCr_2Si_2C$ and $PrCr_2Si_2C$ composition, and to determine the crystallographic direction of the chosen piece of ingot.

All the Laue patterns taken for $LaCr_2Si_2C$ confirmed the polycrystallinity of the whole ingot. The $CeCr_2Si_2C$ ingot was a single crystal of rather low quality – the ingot contained a lot of off-oriented small grains. The best result was obtained for the $PrCr_2Si_2C$ compound. The crystallinity of the ingot was checked, and then the sample was oriented along the (001) and (100) crystallographic direction for further experiments.

5.2.3 Microprobe analysis

The $LaCr_2Si_2C$, $CeCr_2Si_2C$ and $PrCr_2Si_2C$ samples were characterized by SEM. All three samples were found to be single-phased and homogeneous. Moreover, the stoichiometric composition of each sample was determined by EDAX analysis. The error of the particular elements concentrations was about 5 %. The results of EDAX analysis are presented in Table 5.2.

$LaCr_2Si_2C$	At. (%)	$CeCr_2Si_2C$	At. (%)	$PrCr_2Si_2C$	At. (%)
La	16	Ce	20	Pr	15
Cr	35	Cr	34	Cr	39
Si	29	Si	30	Si	26
C	20	C	16	C	20

Table 5.2: The ratio of constituent elements for $LaCr_2Si_2C$, $CeCr_2Si_2C$ and $PrCr_2Si_2C$ compounds obtained by the EDAX analysis.

5.3 RCr_2Si_2 compounds

5.3.1 Specific heat measurements

The specific heat of the RCr_2Si_2 compounds was measured in the zero magnetic field in the temperature range 2–300 K. The error of the experimental data of the specific heat was 0.5–2 % depending on the temperature. The temperature dependencies of the specific heat for $TbCr_2Si_2$ and $ErCr_2Si_2$ are presented in Figs. 5.6 and 5.7, respectively.

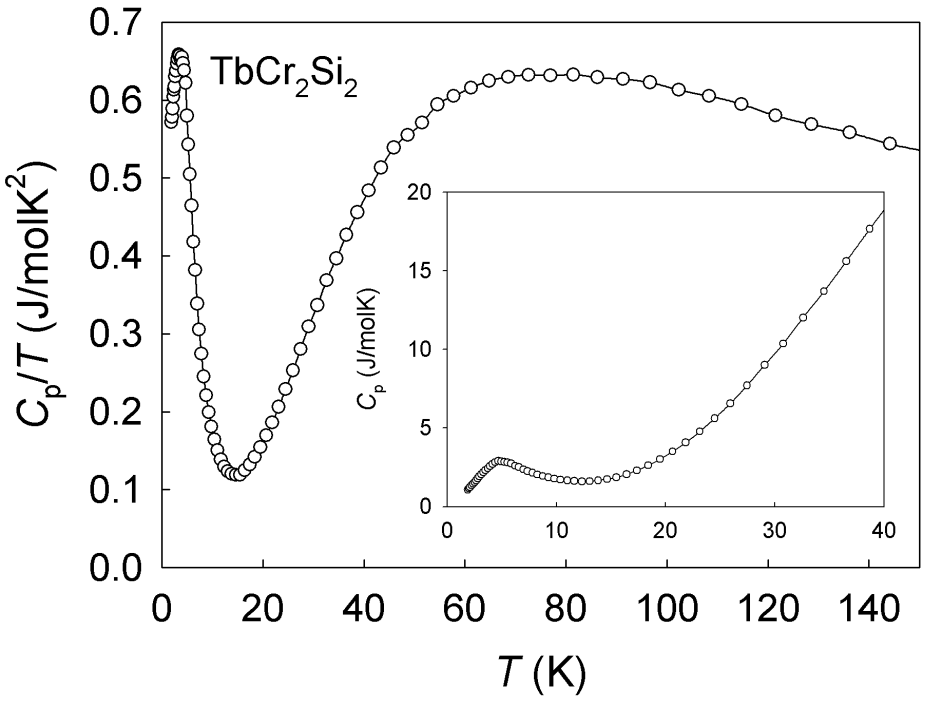

Fig. 5.6: Specific-heat data of $TbCr_2Si_2$.

In the case of $TbCr_2Si_2$ compound, there is a broad anomaly observed at $\sim$ 5.2 K. According to the Ref. [15], the Néel temperature for this compound is about 2.4 K, which agrees with our magnetization data as shown further.

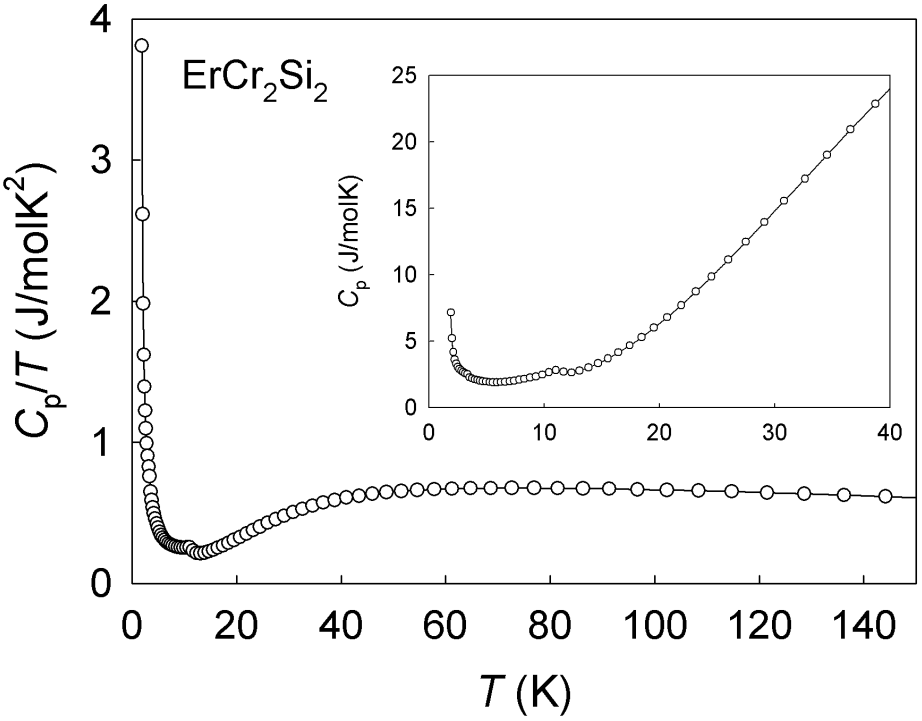

Fig. 5.7: Specific-heat data of $ErCr_2Si_2$.

The discrepancy can be explained as follows.

The anomaly occurs not because of the magnetic ordering only, however, significant contribution due to the lower-lying crystal field levels is present. Therefore, the purely magnetic contribution would be obtained after subtraction of the CF part, and the T_N-related maximum would appear at temperature closer to the proposed Néel temperature. Unfortunately, attempts to obtained proper description of the specific heat failed due to several CF schemes obtained.

For $ErCr_2Si_2$, there is a significant increase of the specific heat below about 6 K. This anomaly can be treated similarly as in the case of Tb compound.

According to the Ref. [15], the Néel temperature is less than 1.6 K. This is also suggested by the measurement of the AC susceptibility discussed in the next section.

An additional minor anomaly is present at around 10 K. Taking into the account the results of magnetization and AC susceptibility measurements, we are not sure about the origin of this effect at the moment. Definitely, it is not a contribution of Er oxide, which ordering temperature is reported as 3.4 K [24]. Probably, it is caused by a short range order of the Er sublattice or by population of the crystal field levels.

We propose to synthesize non-magnetic analogue – $LuCr_2Si_2$, analyze its specific heat in detail, and try to subtract the corresponding contributions to the specific heat for the $TbCr_2Si_2$ and $ErCr_2Si_2$, respectively, more rigorously.

5.3.2 Magnetization measurements

For both compounds, we performed the detailed study by AC susceptibility (in the temperature range 2–40 K), and magnetization measurements (in the temperature range 2–900 K).

The real part of the AC susceptibility as a function of temperature, $\chi'(T)$, is displayed in Fig. 5.8. A broad maximum of the AC susceptibility at ~ 3 K is observed for $TbCr_2Si_2$. According to [15], it may be the indicative of the magnetic ordering of the Tb sublattice to the antiferromagnetic state.

In contrast to the Tb compound, the AC susceptibility of $ErCr_2Si_2$ shows a peak at ~ 2 K, which can be attributed to the magnetic phase transition to the ferromagnetic state according to [18].

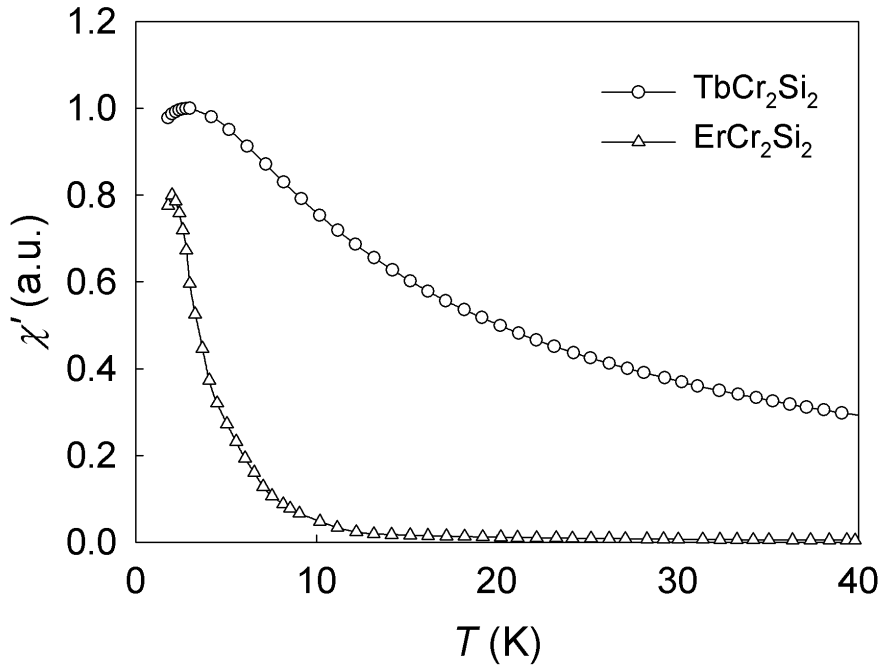

Fig. 5.8: Temperature dependence of the real part of the AC susceptibility for $TbCr_2Si_2$ and $ErCr_2Si_2$.

Figs. 5.9 and 5.10 shows the temperature dependence of the magnetization below 100 K in several magnetic fields for $TbCr_2Si_2$ and $ErCr_2Si_2$, respectively. The low-field curve for $ErCr_2Si_2$ reflects well the AC-susceptibility data. For both compounds, the zero-field-cooled (ZFC) and the field-cooled (FC) curves measured in low field coincide down to 2 K. The magnetization is suppressed with the decreasing magnetic field as expected for ferromagnetic-type of ordering. Except the low temperature ordering-related anomaly, no additional effects were observed at higher temperature.

The high-temperature dependence of magnetization of both compounds is plotted in Figs. 5.11 and 5.12, respectively. We can clearly see, that there are no ano-

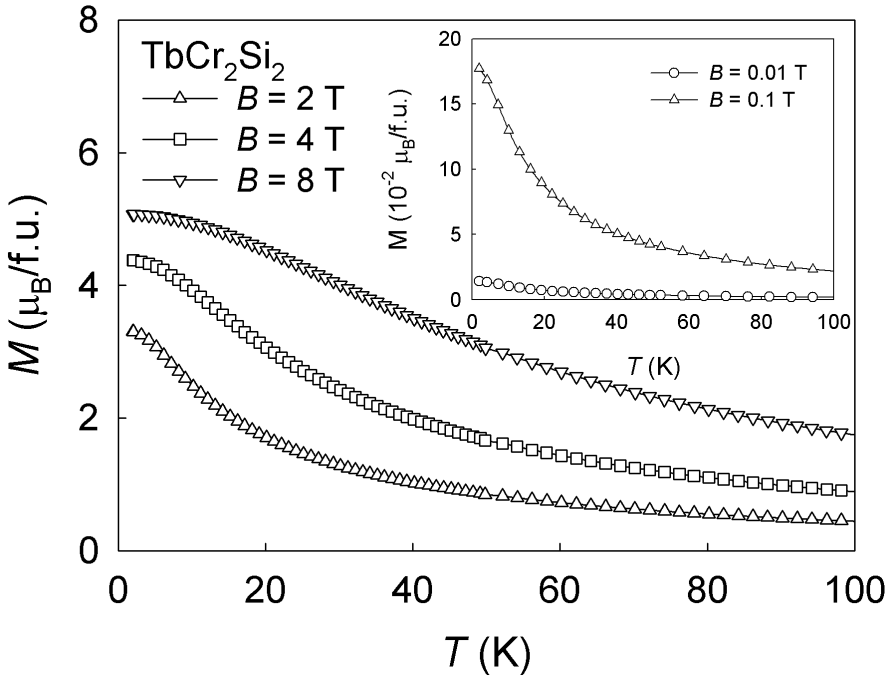

Fig. 5.9: Temperature dependence of the magnetization of $TbCr_2Si_2$.

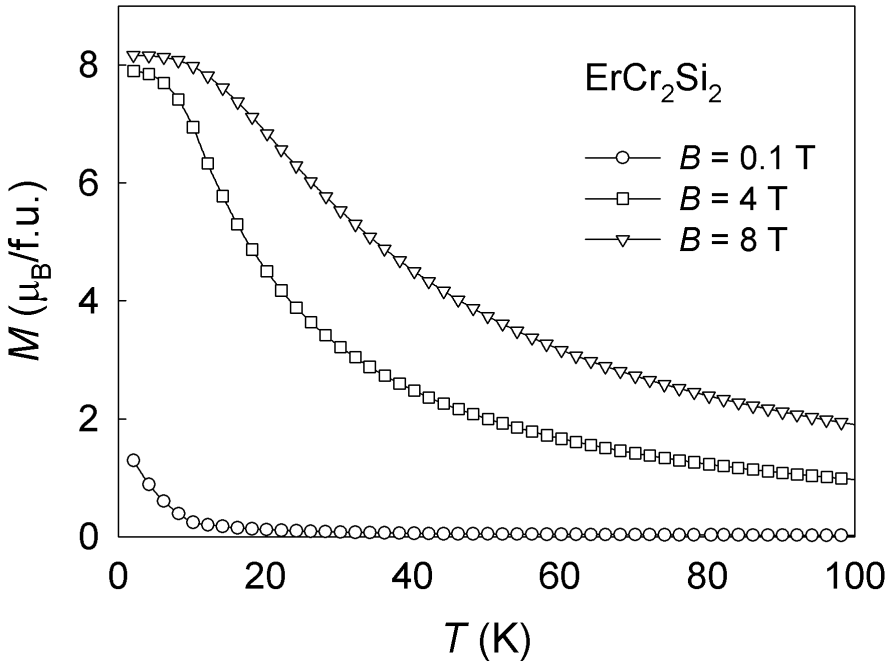

Fig. 5.10: Temperature dependence of the magnetization of $ErCr_2Si_2$.

malies, which could confirm the antiferromagnetic ordering of the Cr sublattice at 758 and 692 K for $TbCr_2Si_2$ and $ErCr_2Si_2$, respectively, according to [18]. As we are sure with the stoichiometry and homogeneity of our samples, we claim, that the Cr sublattice does not order down to low temperatures, however, we cannot exclude simultaneous ordering of the rare-earth and Cr sublattice at ~ 2 K.

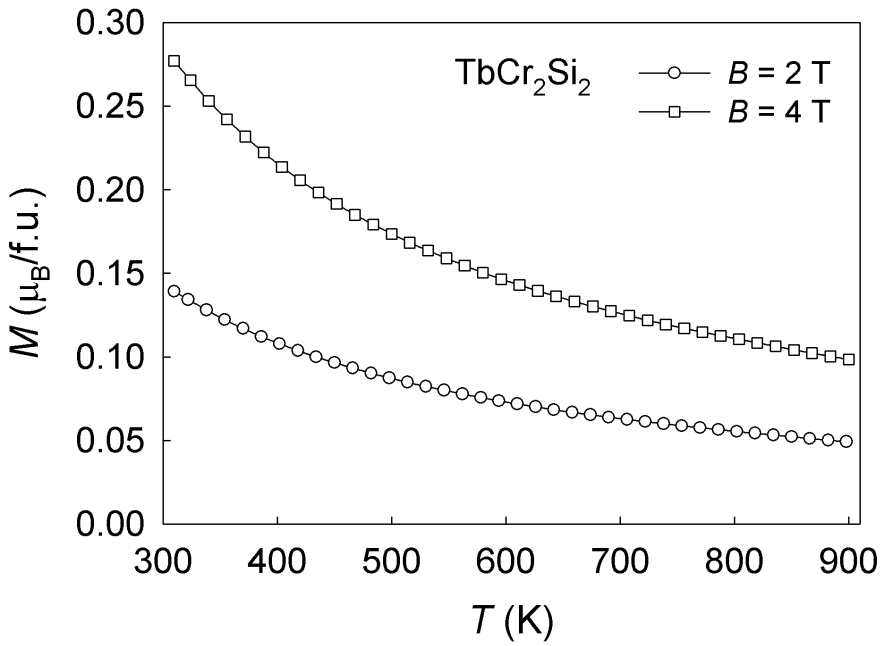

Fig. 5.11: The high-temperature dependence of the magnetization of $TbCr_2Si_2$.

Using the results of magnetization measurement in the wide temperature range (2–900 K), we plotted the temperature dependence of the inverse magnetic susceptibility for both compounds. Both curves were fitted in the high-temperature range (400–900 K) using the modified Curie-Weiss law:

$$\chi = \chi_0 + \frac{C}{T - \theta_\mathrm{p}}. \tag{5.1}$$

The obtained values of the effective moment μ_eff and the paramagnetic Curie temperature θ_p for both compounds are presented in Table 5.3. For $TbCr_2Si_2$, the χ_0 term was found to be negligible, but in the case of the Er compound, it was found to be of the order $10^{-8}\,\mathrm{m^3/mol}$ and was finally included in the fit.

If we compare the values of the effective moment for Tb and Er compounds with the values for the free Tb^{3+} and Er^{3+} ions, respectively, we can see that for both compounds, there is some additional paramagnetic contribution, which may be attributed to the Cr sublattice.

It is important to mention, that the results in Table 5.3 were obtained by the fit of the high-temperature data. We also fitted the low-temperature data obtaining a bit higher values of the θ_p (-6 K and 6 K for $TbCr_2Si_2$ and $ErCr_2Si_2$,

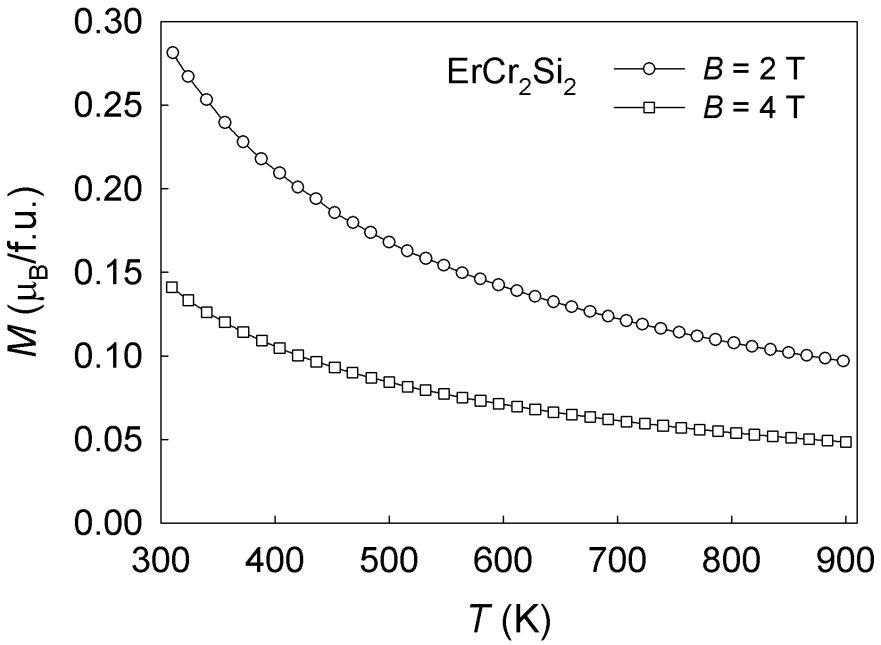

Fig. 5.12: The high-temperature dependence of the magnetization of $ErCr_2Si_2$.

respectively), and the effective moment of 10.0 and 9.7μ_B/f.u. for $TbCr_2Si_2$ and $ErCr_2Si_2$, respectively.

RCr_2Si_2	χ_0 (m^3/mol)	θ_p (K)	μ_{eff} (μ_B/f.u.)	theor. μ_{eff} (μ_B/f.u.)
$TbCr_2Si_2$	$(0.9 \pm 0.1) \cdot 10^{-10}$	-28 ± 5	10.1 ± 0.5	9.72
$ErCr_2Si_2$	$(1.1 \pm 0.2) \cdot 10^{-8}$	-18 ± 4	9.8 ± 0.5	9.59

Table 5.3: The values of the χ_0 term, the effective moment and the paramagnetic Curie temperature obtained for RCr_2Si_2 samples by fitting the $1/\chi(T)$ curve to the Curie-Weiss law. The theoretical values of the effective moment for the free R^{3+} ion is also presented.

It is caused by the fact, that the high-temperature $1/\chi(T)$ curves for both compounds are not linear. The low-temperature data were recorded on powders, where the magnetic moments are randomly oriented. The high-temperature data were measured on bulk pieces, where the preferential orientation of crystallites results in dominant contribution of one axis - we expect contribution of the crystal field, which causes curvature of the susceptibility curves. Therefore, the results of the high-temperature fit depend on the orientation of the bulk piece with respect to the applied magnetic field during the measurement.

Let's briefly discuss our results in context of the magnetic structure obtained by Moze et al. [18]. They proposed antiferromagnetic ordering of the Cr sublattice with magnetic moment aligned along the c-axis, and ferromagnetic ordering of the Er moments parallel to the a-axis. If we stand out on the lack of ordering of the Cr

sublattice, the obtained negative values of θ_p suggests, that the antiferromagnetic exchange is dominant in both compounds.

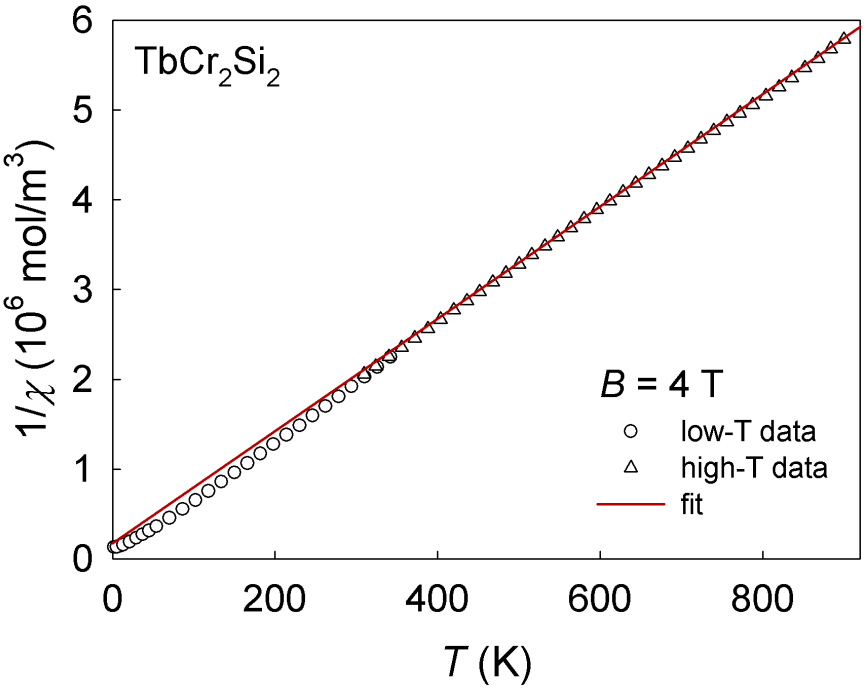

Fig. 5.13: Temperature dependence of the inverse magnetic susceptibility of $TbCr_2Si_2$ measured at 4 T.

The evolution of the magnetization isotherms of the both samples with respect to temperature is displayed in Figs. 5.15 and 5.16.

The Tb compound exhibit the value of the magnetic moment of $5\mu_B$/f.u. at 2 K and 9 T, which continuously decreases down to $4\mu_B$/f.u. at 30 K. Closer inspection of the magnetization curves for $TbCr_2Si_2$ reveals a remnant of metamagnetic transition into a field-induced ferromagnetic state. For better insight into the effect, we constructed the Arrott-plot for $TbCr_2Si_2$ (Fig. 5.17). The 2 K curve shows a suspicion of S-shape in low fields. Considering the ordering temperature about 2 K and measurement on powder sample, we assume, that the metamagnetic transition must not necessarily results into a significant sharp step in magnetization curve. Similar character of metamagnetic transition was observed in isostructural $TbFe_2Si_2$ [25].

At the temperature 2 K, the $ErCr_2Si_2$ compound shows a saturation already at 2 T with the saturation moment of about $8.1\mu_B$/f.u.. The values of remanence, M_r, and coercivity, H_C, were determined as: $M_r \sim 0.33\mu_B$/f.u. and $H_C \sim 0.01$ T. The results of the saturated magnetic moment are in discrepancy with the values presented by Moze et al. The ordered moment on Er is reported to be $5.25\mu_B$ only. If we assume simultaneous ordering of the Cr sublattice, and considering

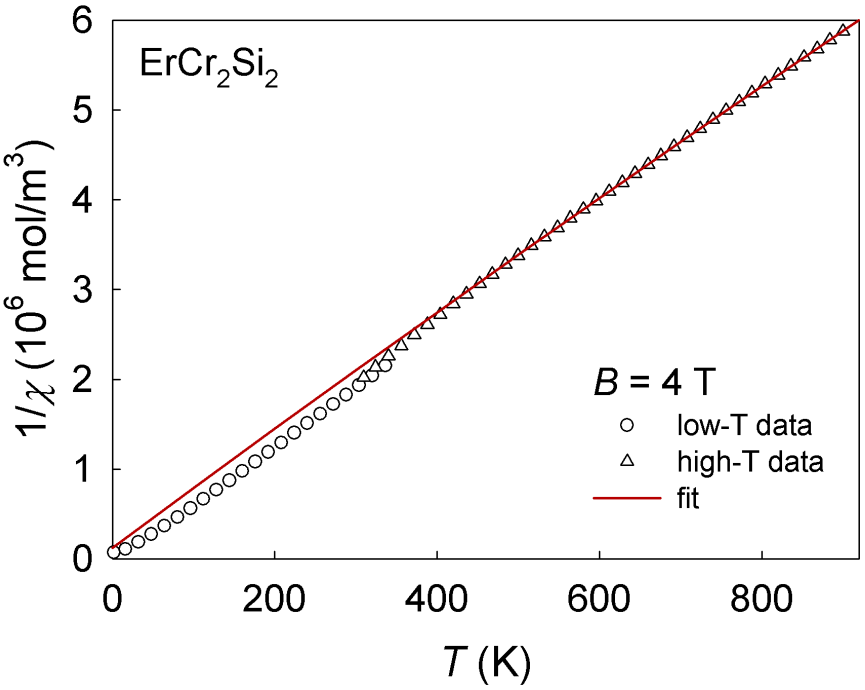

Fig. 5.14: Temperature dependence of the inverse magnetic susceptibility of $ErCr_2Si_2$ measured at 4 T.

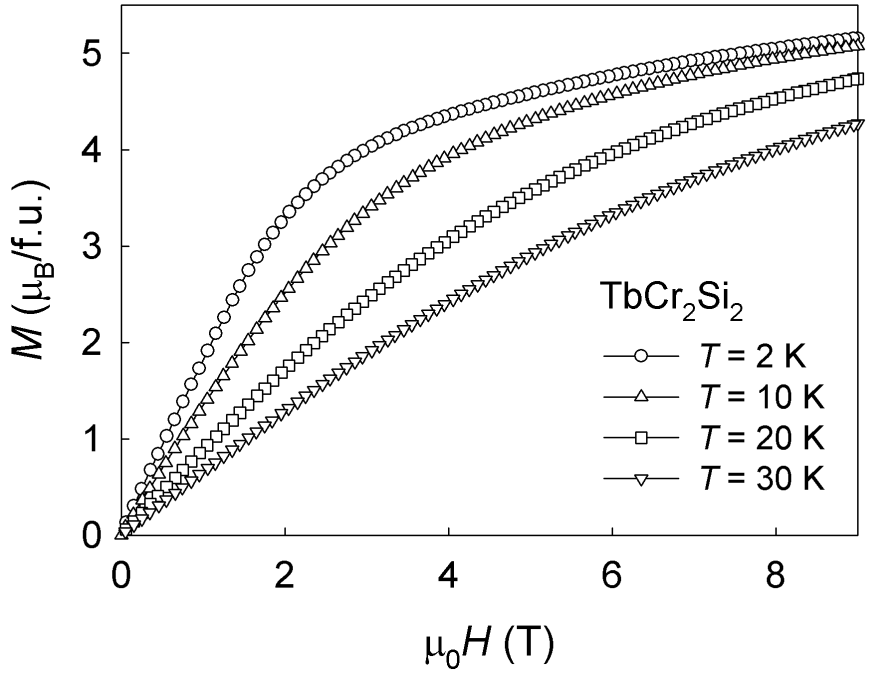

Fig. 5.15: Magnetization isotherms measured on the $TbCr_2Si_2$ sample at various temperatures.

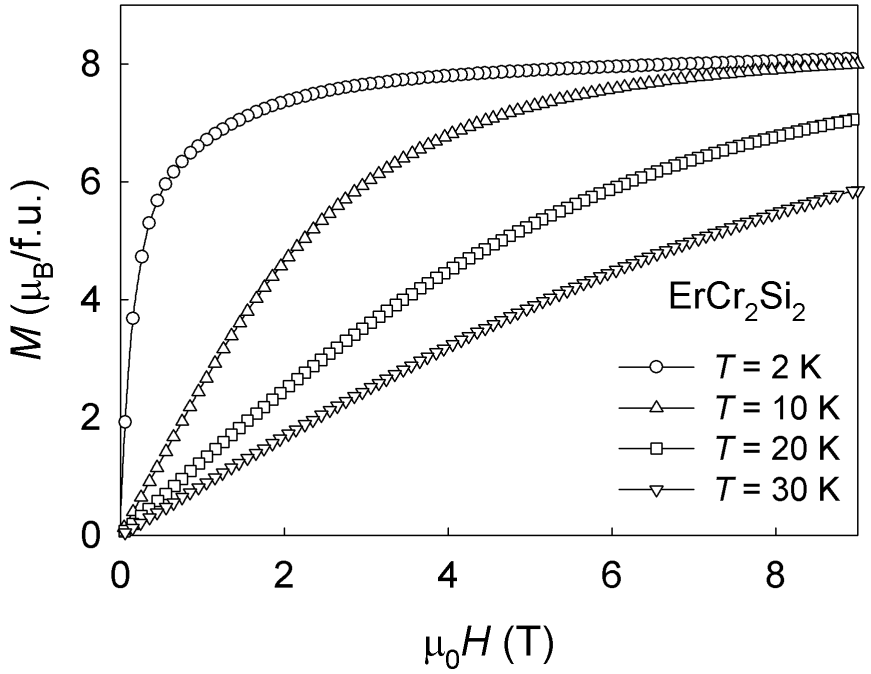

Fig. 5.16: Magnetization isotherms measured on the $ErCr_2Si_2$ sample at various temperatures.

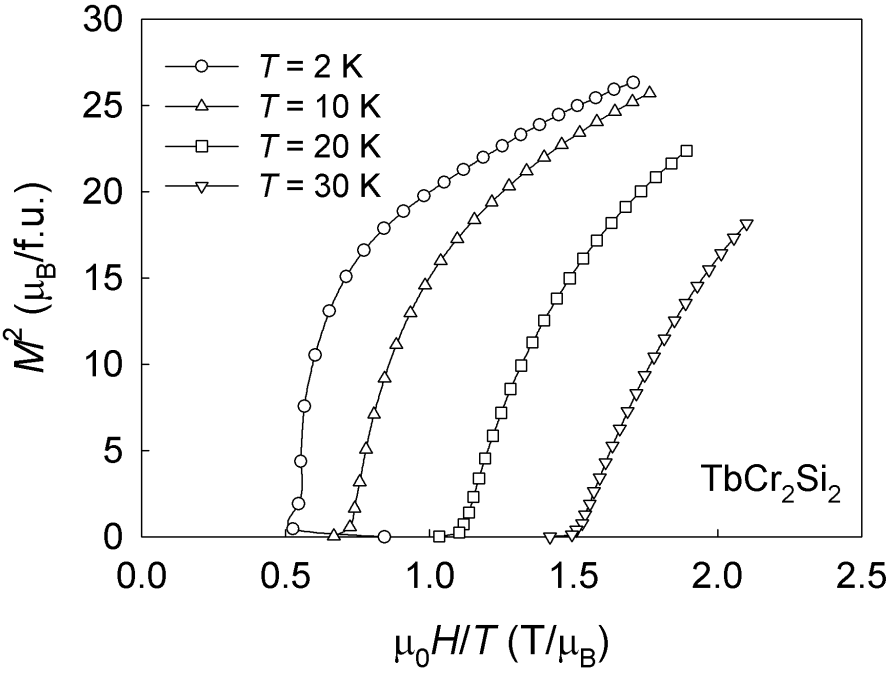

Fig. 5.17: Arrott plots for $TbCr_2Si_2$.

the reported magnetic moment for Cr $1.36\mu_B$, our results are still in discrepancy with the reported magnetic structure.

Therefore, detailed studies of magnetic ordering in both compounds on single crystals are desirable in order to determine the proper magnetic structures.

5.4 RCr_2Si_2C compounds

5.4.1 Specific heat measurements

The specific heat of all studied polycrystalline samples was measured at zero magnetic field in the temperature range 2–300 K. Moreover, we performed the measurement of the $PrCr_2Si_2C$ single crystal along the c-axis at various magnetic fields in the temperature range 2–150 K.

The temperature dependencies of the specific heat measured at zero magnetic field for all studied samples are presented in Fig. 5.18. No significant anomalies are found for $LaCr_2Si_2C$ and $CeCr_2Si_2C$. For $PrCr_2Si_2C$ and $NdCr_2Si_2C$, we observe the $C_p(T)$ anomaly at about 30 K and 21 K, respectively. Taking into account the results of magnetization and AC susceptibility measurements discussed further, we attribute these anomalies to a magnetic phase transition at the Curie temperature T_C, below which the Pr and Nd sublattice orders ferromagnetically.

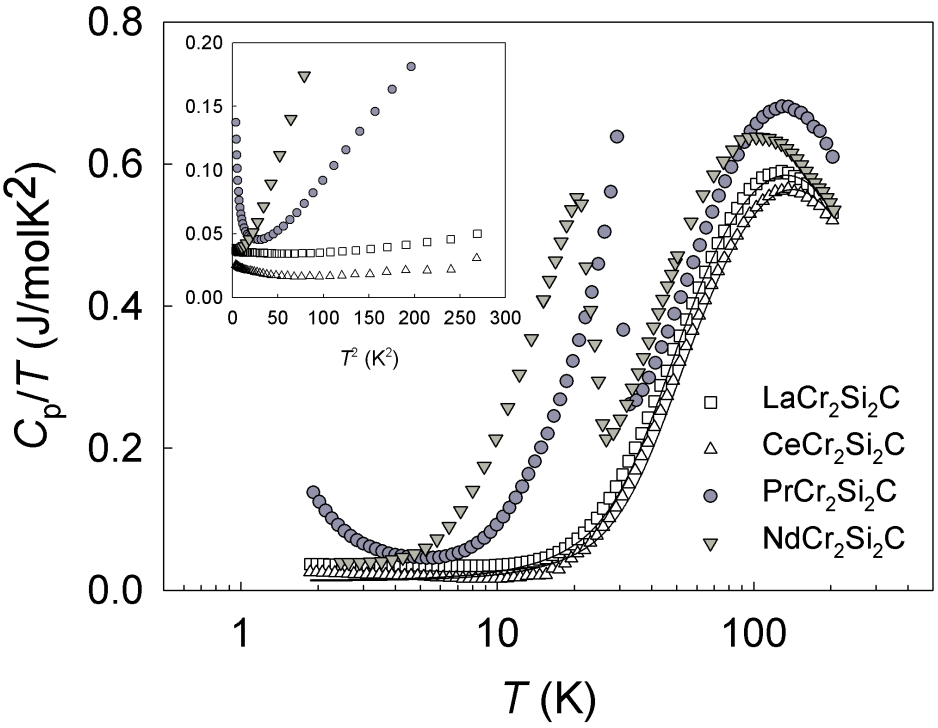

Fig. 5.18: Specific heat data of the RCr_2Si_2C compounds. The full lines represent the fit.

The specific-heat data were further analyzed as a sum of different relevant contributions (see section 2.5). Since the corresponding data for the La and Ce compounds do not deviate significantly, we may assume that, in both compounds, there are just two contributions to the total specific heat: one arising from the conduction electrons and one from the phonons.

In these compounds, the phonon spectrum consists of three acoustic branches and 15 optical branches. The specific-heat data were fitted to the formula (2.33), section 2.5.2. The electronic contribution was treated within the Sommerfeld model. The fits to the $LaCr_2Si_2C$- and $CeCr_2Si_2C$-data are represented by full lines in Fig. 5.18 and all fitted parameters are listed in Table 5.4 (the anharmonic corrections have not been included in the analysis). Below about 20 K, the specific heat could not completely be described by the proposed model. There is evidence of an additional contribution of speculative origin. The inset in Fig. 5.18 demonstrates a significant deviation from the expected linear C_p/T vs T^2 dependence below 20 K in the form of a low-temperature up-turn below 10 K. Because, as will be shown in the next section, also the magnetic susceptibility exhibits low temperature anomalies, the enhancement of the low-T specific heat may be related to the magnetic behavior of the Cr sublattice.

RCr_2Si_2C	γ (mJ/molK^2)	θ_D (K)	n_1	θ_{E1} (K)	n_2	θ_{E2} (K)	n_3	θ_{E3} (K)	n_4	θ_{E4} (K)
$LaCr_2Si_2C$	14	252	3	611	6	554	3	236	3	308
$CeCr_2Si_2C$	13	278	3	617	6	563	3	247	3	328

Table 5.4: Results of the specific-heat analysis for $LaCr_2Si_2C$ and $CeCr_2Si_2C$. n is the degeneracy of the phonon branches.

The specific heat of $PrCr_2Si_2C$ exhibits, beside the phonon and electron contributions, an additional contribution to the specific heat above 30 K, which can be attributed to the crystal field acting on the Pr ion. Same effect is observed above 21 K for $NdCr_2Si_2C$. However, analyzing this part in terms of a Schottky anomaly was not unambiguous because it yields several possible crystal-field level schemes. The low-T upturn of the C_p/T vs T^2 curve of the $PrCr_2Si_2C$ (inset in Fig. 5.18) may be due to an additional phase transition below 2 K or rather to a nuclear contribution of the Pr^{3+} ion.

The temperature dependence of the estimated magnetic entropy S_{mag} (obtained after subtracting the electron and phonon parts, respectively) for $PrCr_2Si_2C$ is represented in Fig. 5.19. Slightly below T_C, S_{mag} reaches a value of about $R\ln 2$ and, at about 250 K, it saturates at $R\ln 9$, which is the value expected for the Pr^{3+} ion.

For the $PrCr_2Si_2C$ single crystal, we also performed the measurement of the specific heat along the c-axis in magnetic fields 0 T, 0.25 T, 1 T and 5 T in the temperature range 2–150 K. The measured data are presented in Fig. 5.20.

As mentioned above, the zero-field curve shows a considerable anomaly at

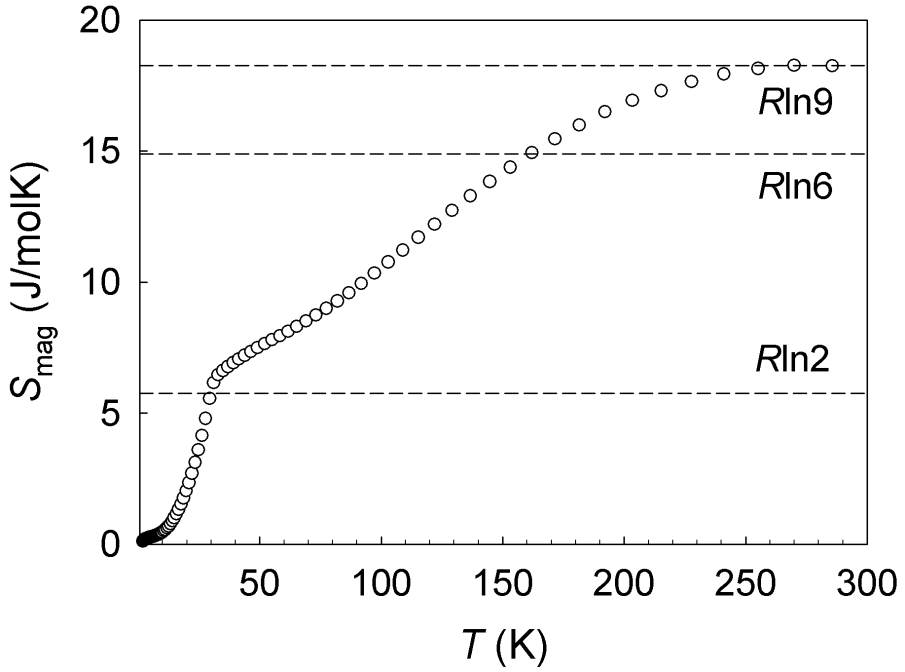

Fig. 5.19: Temperature dependence of the magnetic part of the entropy for $PrCr_2Si_2C$.

about 30 K which is caused by the magnetic phase transition to the ferromagnetic state below 30 K. This anomaly is suppressed with the increasing applied magnetic field. On the basis of the measured data we calculated the entropy change of the sample for various magnetic-field changes, which is plotted in Fig. 5.21. We can see that $(-\Delta S)$ always shows the maximum $(-\Delta S_{\max})$ at T_C as expected for a ferromagnet. The value of $(-\Delta S_{\max})$ rapidly increases with the increasing magnetic-field change. The maximum value of the entropy change in $\Delta B = 5\,\mathrm{T}$ is $(-\Delta S_{\max}) = 2.75\,\mathrm{J/molK}$.

5.4.2 Magnetization measurements

For all four studied compounds, the detailed magnetization study was performed in the temperature range 2–900 K. Moreover, we performed the magnetization measurements for $CeCr_2Si_2C$ and $PrCr_2Si_2C$ singlecrystals with expectation of the strong magnetocrystalline anisotropy present in the sample.

AC-susceptibility measurements

The real part of the AC susceptibility as a function of temperature, $\chi'(T)$, is displayed in Fig. 5.22 for all four compounds. The large symmetric peak at about 30 K for $PrCr_2Si_2C$ coincides with the C_p/T anomaly. For $NdCr_2Si_2C$ compound, we observe a double peak with maximum at about 22 K and a shoulder at

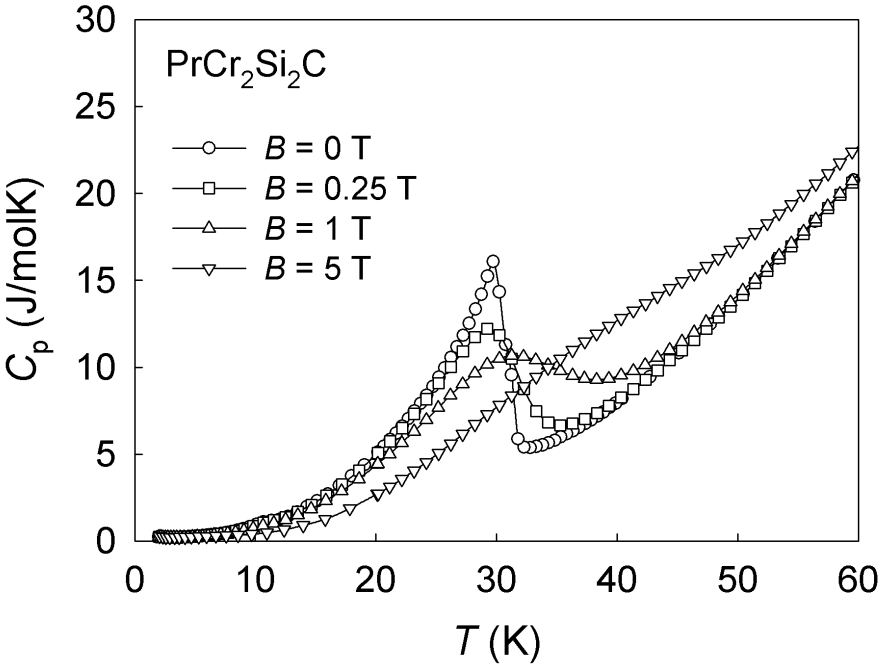

Fig. 5.20: Temperature dependencies of the specific heat of $PrCr_2Si_2C$ single crystal measured along the c-axis in different magnetic fields up to 5 T.

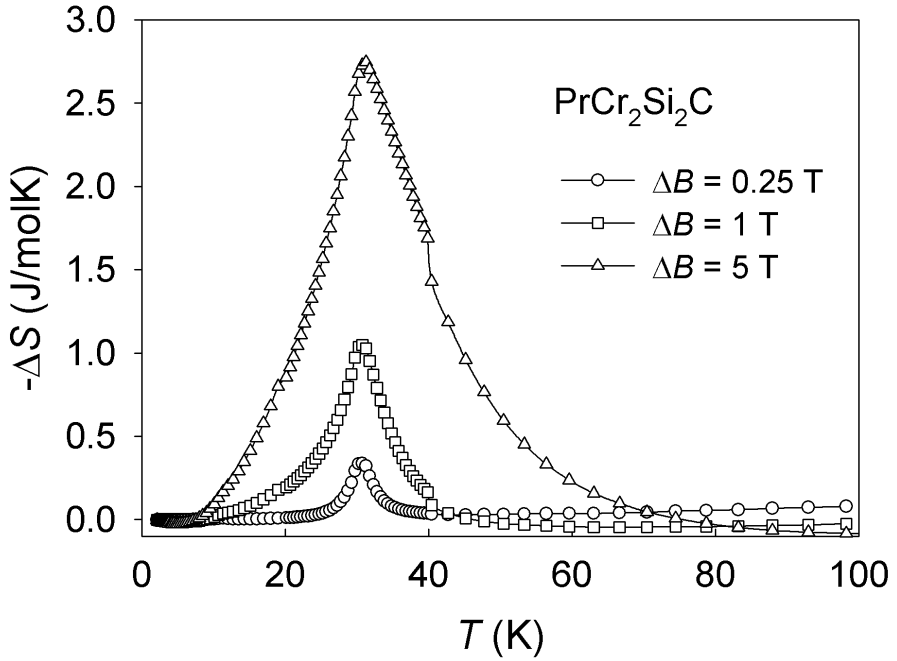

Fig. 5.21: Entropy change of $PrCr_2Si_2C$ single crystal for the various magnetic-field changes determined from the specific-heat data.

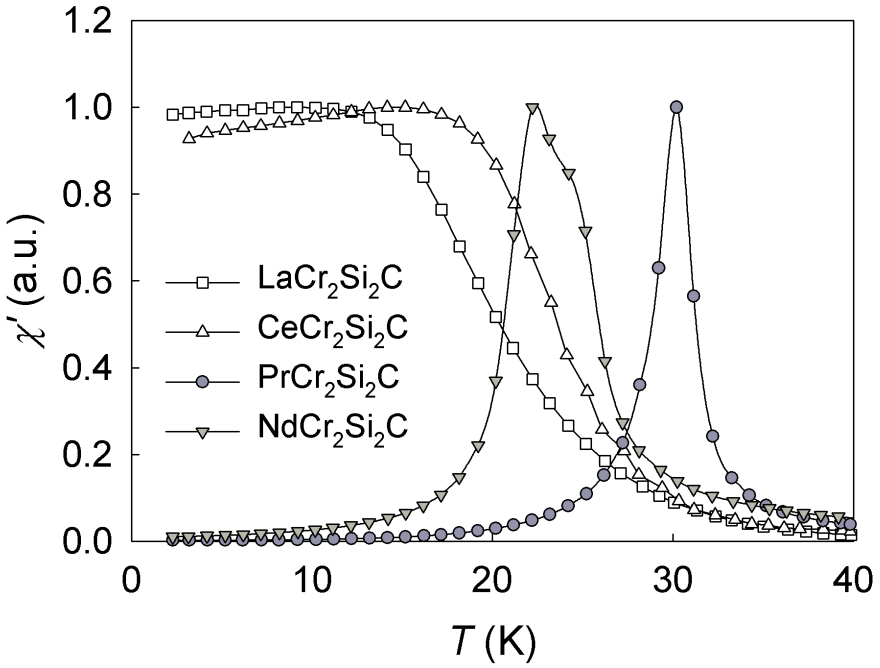

Fig. 5.22: The temperature dependence of the real part of the AC susceptibility for RCr_2Si_2C.

about 24 K.

The $\chi'(T)$ curves for $LaCr_2Si_2C$ and $CeCr_2Si_2C$ do not show a peak, however, a sudden increase is observed below about 30 K with inflection points at 18 and 22 K, respectively, reaching broad maxima around 15 and 18 K, respectively. Upon further cooling, χ' slightly decreases.

For $PrCr_2Si_2C$ single crystal, the AC susceptibility was measured along the a- and c-axis, respectively. The results of the measurement along the c-axis are presented in Figs. 5.23 and 5.24. The AC susceptibility reaches the maximum at $T_C = 30$ K for $f = 1$ Hz. This position of the maximum is almost intact with change of the applied AC frequency (shifted to 30.3 K for $f = 1$ kHz only). However, for the increasing frequencies, the tapering of the peaks is observed. The results of the measurement along the a-axis are very similar to those measured along the c-axis, but with nearly five-times smaller values of the AC susceptibility. It supports the fact, that the c-axis is the easy magnetization axis in the system.

The imaginary component of the AC susceptibility, χ'', in general indicates dissipative processes in the studied sample. A nonzero imaginary susceptibility in $PrCr_2Si_2C$ (Fig. 5.24) indicates irreversible domain wall movement, accompanied with the energy absorption due to a permanent moment. The shift of the maximum, ΔT_C on the χ'' per 10^3 Hz is about 2 K. It can be caused by the dynamics of the domain walls, which occurs within the probed frequency/energy scale.

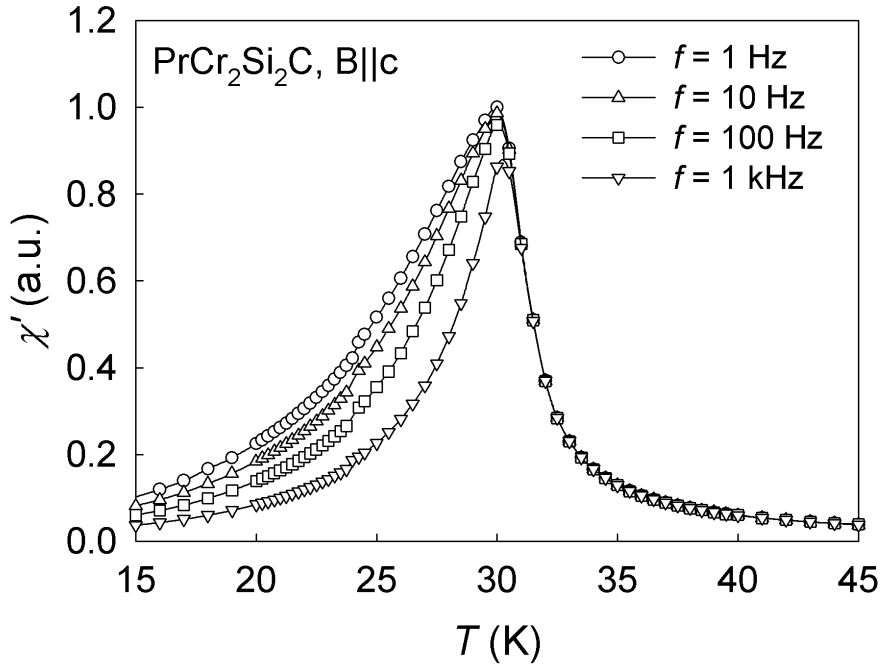

Fig. 5.23: The temperature dependence of the real part of the AC susceptibility for $PrCr_2Si_2C$ single crystal measured along the c-axis at various frequencies.

Magnetization measurements

First, the detailed study of the $M(T)$ dependence was performed for all polycrystalline samples. For the $LaCr_2Si_2C$ and $CeCr_2Si_2C$ compounds, the low-field curve of the temperature dependence of the magnetization agrees well with the AC-susceptibility data (Figs. 5.25 and 5.26). The ZFC and the FC curves measured in low field coincide down to 2 K. The 4 T curve of $LaCr_2Si_2C$ reflects the character of the low-field data as a smooth inflection at around 40 K.

In contrast, the $M(T)$ dependence for $CeCr_2Si_2C$ measured in 4 T increases below about 40 K resulting in a net saturation at very low temperatures. The 2 T curve exhibits an anomaly around 30 K, which may be attributed to an order-to-order magnetic phase transition of predominantly antiferromagnetic character. At closer inspection, the 4 T curve may be considered as somewhat similar to the 2 T curve, being shifted to lower temperatures. An explanation of this may be obtained from a neutron-scattering experiment at low temperatures in the relevant magnetic fields. The very similar low-field magnetization and AC-susceptibility behavior of $LaCr_2Si_2C$ and $CeCr_2Si_2C$, together with the very low values of the magnetic moment at low temperatures suggest a non-magnetic Ce^{4+} ionic state rather than Ce^{3+} in the latter compound.

In contrast to the La and Ce compounds, the ZFC and FC magnetization curves for $PrCr_2Si_2C$ (Fig. 5.27) furcate at $\sim T_C$. We observe the same effect for the $NdCr_2Si_2C$ compound (Fig. 5.28). The higher-field magnetization data

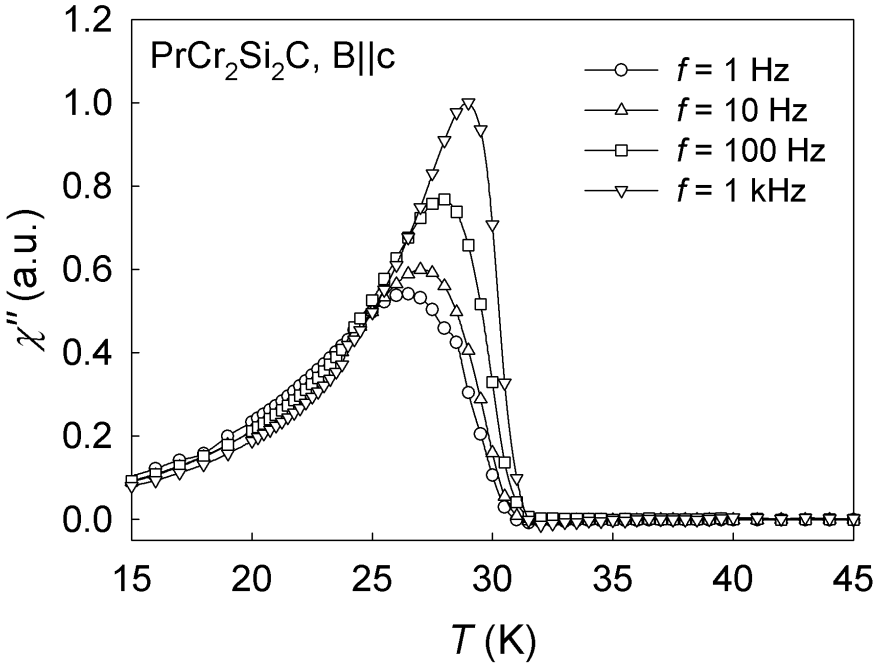

Fig. 5.24: The temperature dependence of the imaginary part of the AC susceptibility for $PrCr_2Si_2C$ single crystal measured along the c-axis at various frequencies. The maximum value of the $\chi''(T)$ is nearly six-times smaller than the maximum value of the $\chi'(T)$.

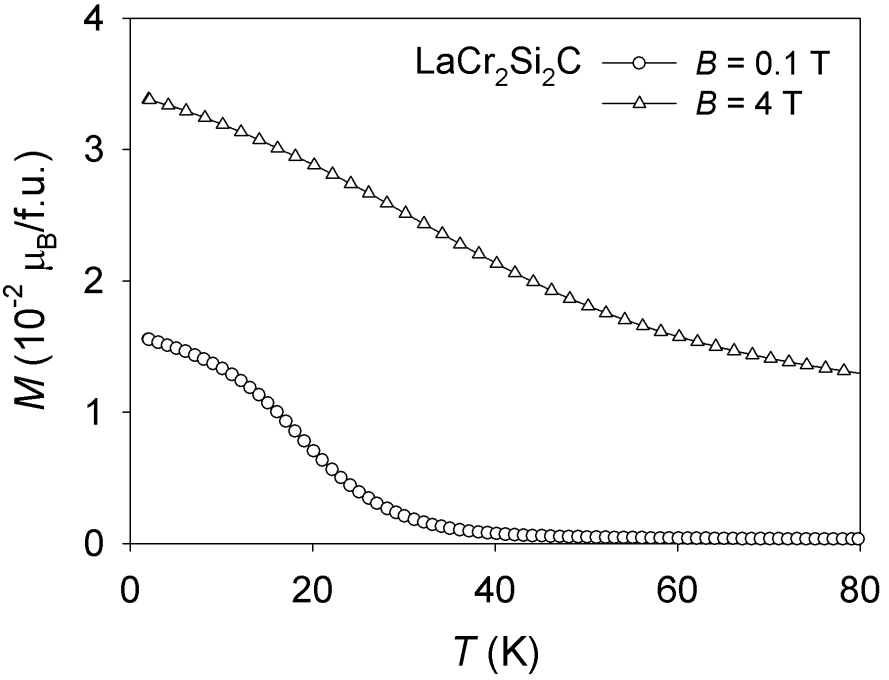

Fig. 5.25: Temperature dependence of the magnetization of $LaCr_2Si_2C$.

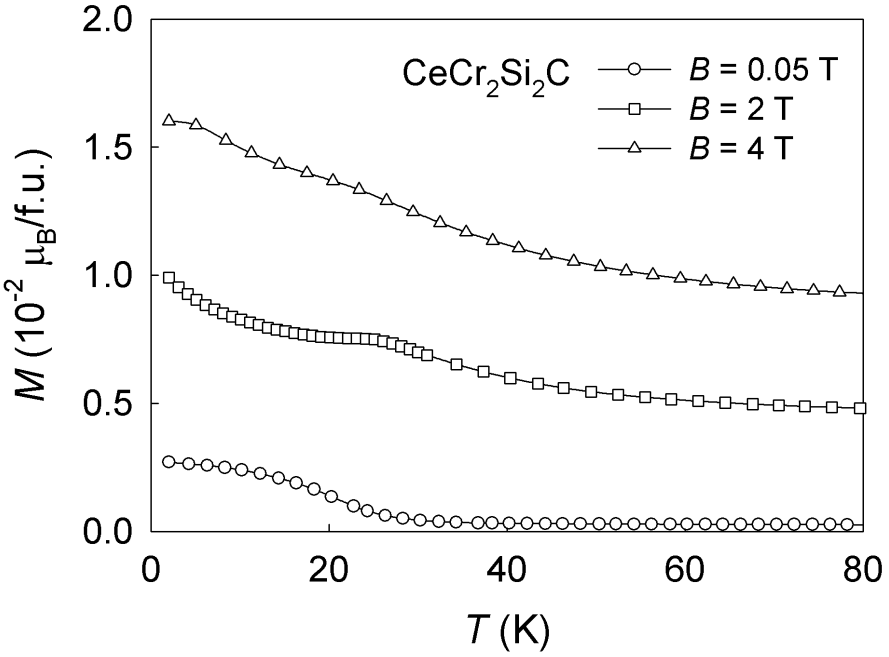

Fig. 5.26: Temperature dependence of the magnetization of $CeCr_2Si_2C$.

for $PrCr_2Si_2C$ coincide below 20 K suggesting rapid saturation of the magnetic moment at magnetic fields larger than 2 T.

For $LaCr_2Si_2C$ and $NdCr_2Si_2C$ polycrystalline samples, we measured the high-temperature dependence of the magnetization in magnetic fields 0.1 T, 2 T and 4 T. No anomalies of $M(T)$ dependencies are observed for both samples, which indicates that no high-temperature ordering of Cr sublattice occurs in both compounds.

The plot of the inverse magnetic susceptibility exhibits a strong deviation from the Curie-Weiss behavior in the La and Ce compound as expected (Figs. 5.31 and 5.32). The La compound exhibits the Pauli-type paramagnetism, and the Ce compound is reported as a valence fluctuator.

In contrast to the La and Ce compounds, the curve for the $PrCr_2Si_2C$ (see Fig. 5.33) could successfully be fitted using the modified Curie-Weiss law (5.1). We obtained an effective magnetic moment value of $(4.0 \pm 0.1)\mu_B$/f.u. and a paramagnetic Curie temperature $\theta_p = (33 \pm 5)$ K. The χ_0 term was found to be of the order 10^{-11} m^3/mol and could be neglected. The enhanced value of the effective magnetic moment with respect to the theoretical value for the free Pr^{3+} ion ($3.58\mu_B$/f.u.) suggests an additional contribution beside the localized Pr moments. One possibility may be a contribution of the Cr sublattice.

The $1/\chi$ curve for $NdCr_2Si_2C$ is not linear in the whole temperature range, a small curvature is observed, which is probably due to the crystal field acting on the rare-earth ions. Moreover, it is an indicative of the magnetocrystalline

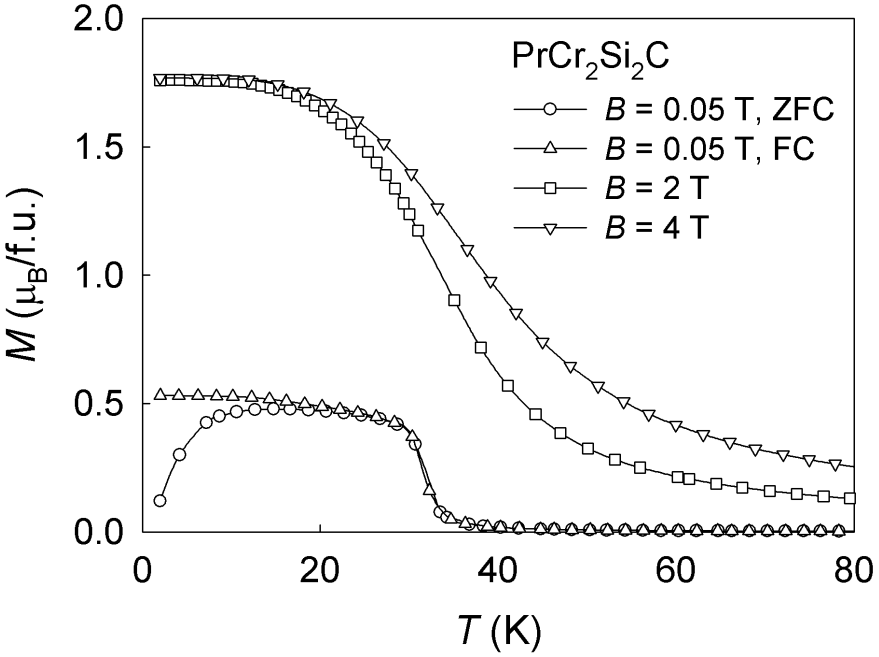

Fig. 5.27: Temperature dependence of the magnetization of $PrCr_2Si_2C$.

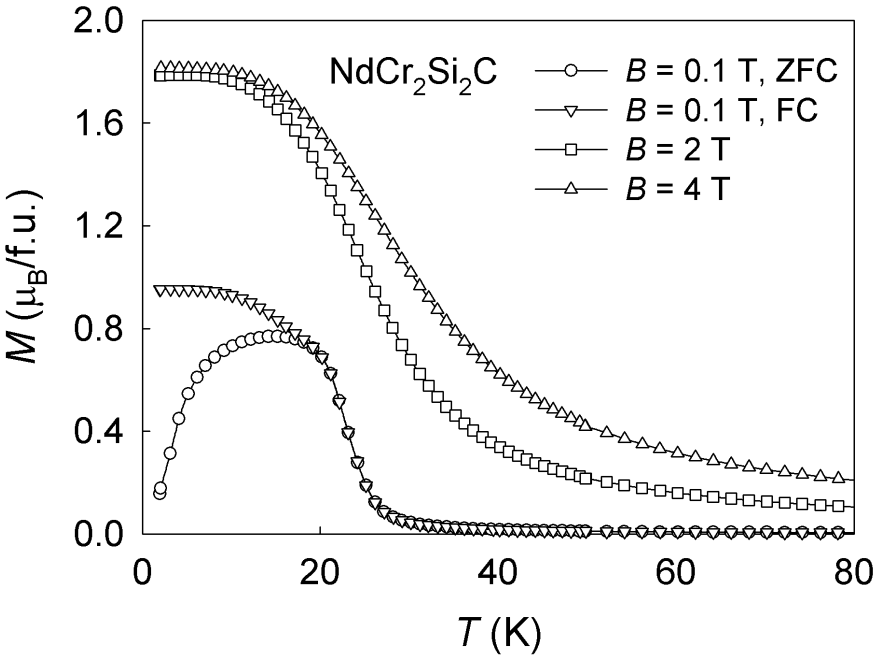

Fig. 5.28: Temperature dependence of the magnetization of $NdCr_2Si_2C$.

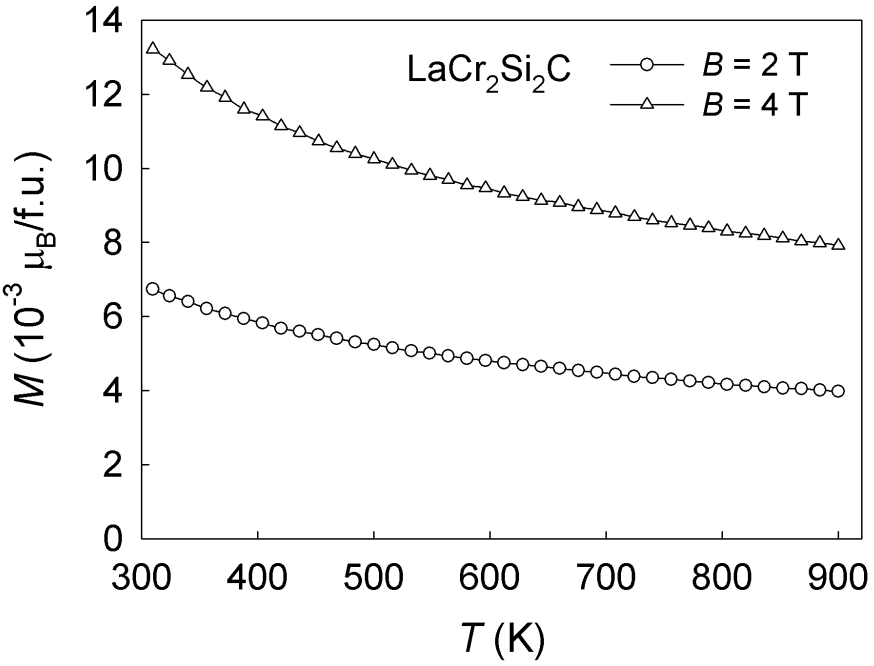

Fig. 5.29: The high-temperature dependence of the magnetization of $LaCr_2Si_2C$.

anisotropy present in the material. Thus the inverse susceptibility of $NdCr_2Si_2C$ was not fitted to Eq. (5.1).

For all studied samples, we measured the $M(H)$ dependence at various temperatures. The $LaCr_2Si_2C$ curves (Fig. 5.35) may comprise two contributions: one rapidly saturating with saturation moment $0.018\mu_B$/f.u. at 2 K and an additional linear term. The situation is similar in the $CeCr_2Si_2C$ case. A net contribution of $\mu_s \sim 0.004\mu_B$/f.u. at 2 K is superimposed on the linear term. In addition, at 2 K a broad metamagnetic anomaly is seen around 1.5 T, which is shifted to about 2.5 T at 10 K. All results obtained on $LaCr_2Si_2C$ and $CeCr_2Si_2C$ indicate the existence of magnetism of the Cr sublattice with a very small spontaneous magnetization below 30 K.

In contrast, at 2 K, the Pr and Nd compounds show a strong ferromagnetic component and rapid saturation already at 0.5 T. The hysteresis loops for both compounds are presented in Figs 5.39 and 5.40. The obtained values of coercivity H_C, remanence M_r and saturation moment μ_s at 2 K for each compound are listed in Table 5.5. For both compounds, the value of M_r decreases with increasing temperature and vanishes at the Curie temperature.

The obtained values of the saturation moment for Pr and Nd compounds are considerably smaller than theoretical values for the free R^{3+} ions. But if we assume that $PrCr_2Si_2C$ and $NdCr_2Si_2C$ exhibit strong magnetocrystalline anisotropy, similar to majority of the RT_2Si_2 compounds, we can estimate that the

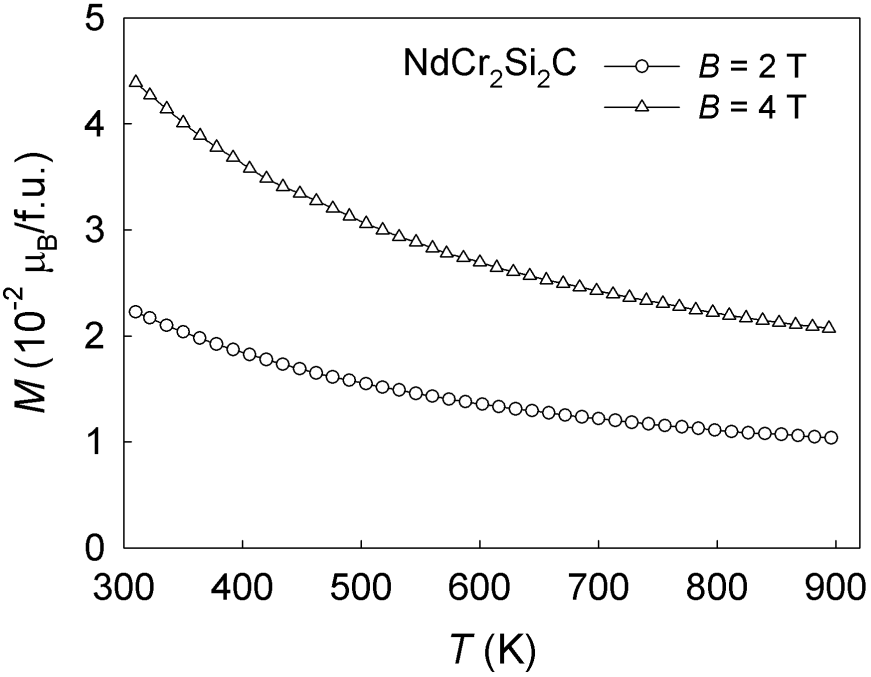

Fig. 5.30: The high-temperature dependence of the magnetization of $NdCr_2Si_2C$.

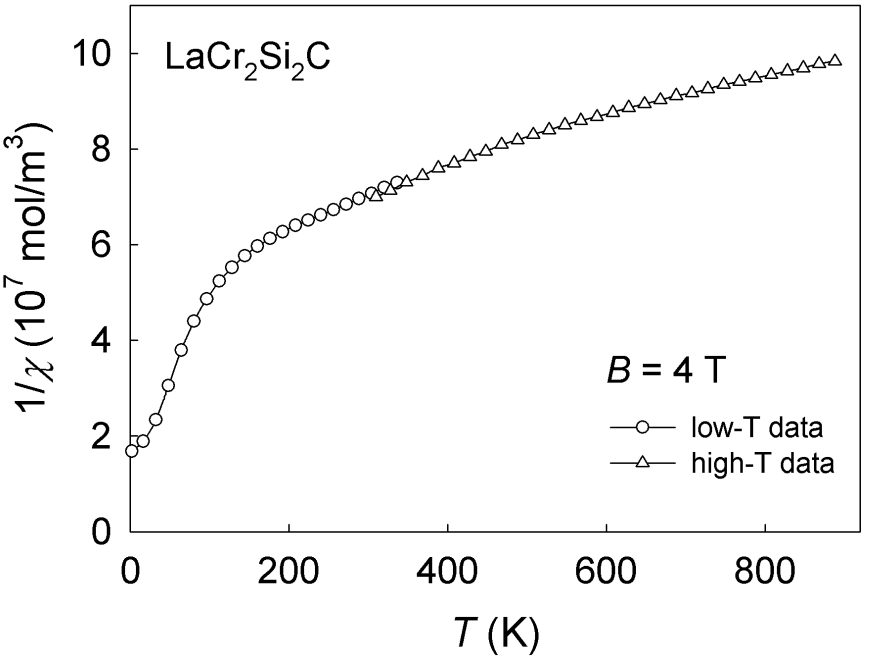

Fig. 5.31: Temperature dependence of the inverse magnetic susceptibility of $LaCr_2Si_2C$ measured at 4 T.

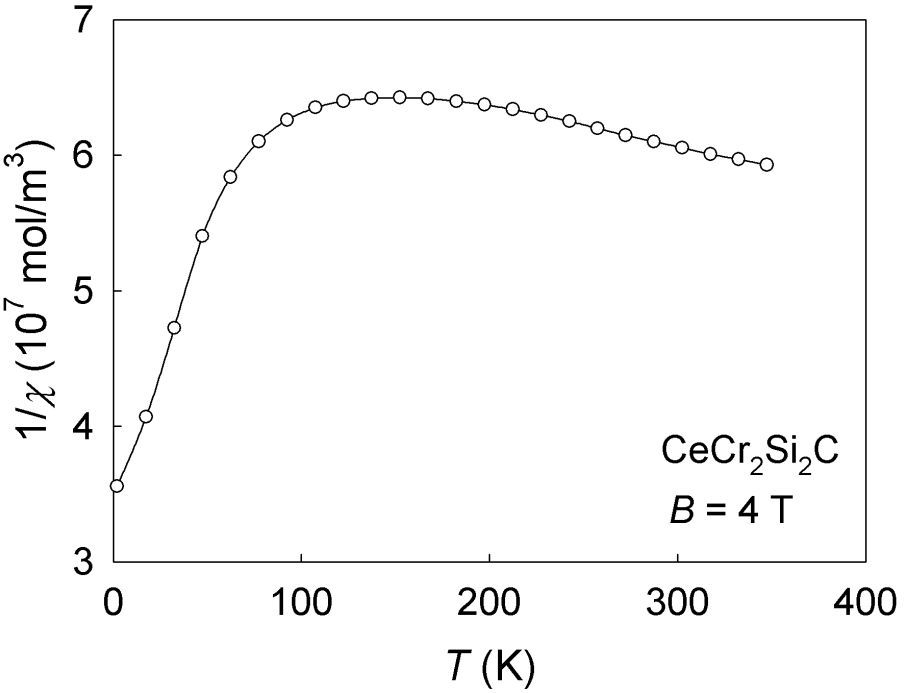

Fig. 5.32: Temperature dependence of the inverse magnetic susceptibility of $CeCr_2Si_2C$ measured at 4 T.

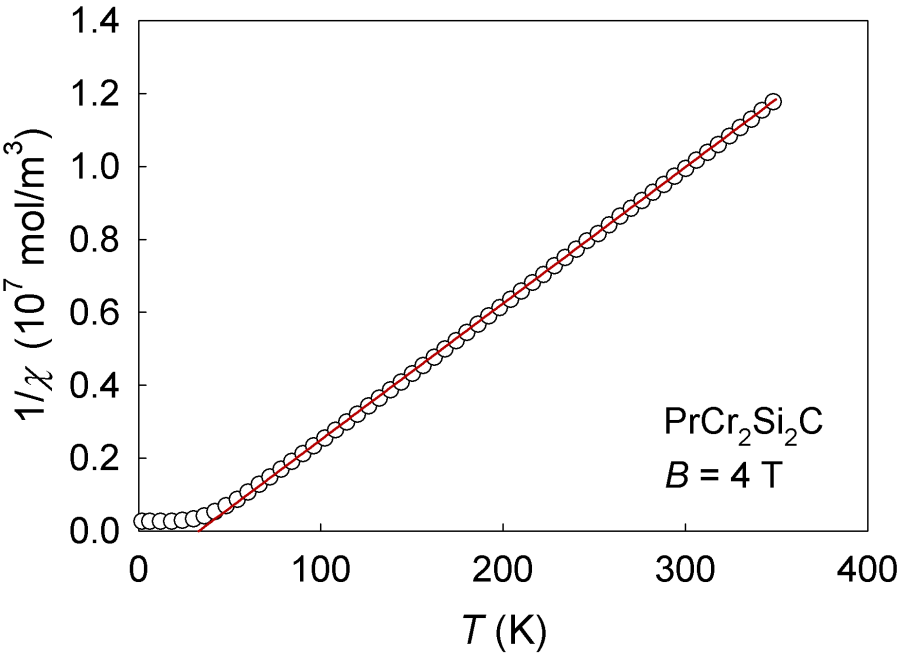

Fig. 5.33: Temperature dependence of the inverse magnetic susceptibility of $PrCr_2Si_2C$ measured at 4 T.

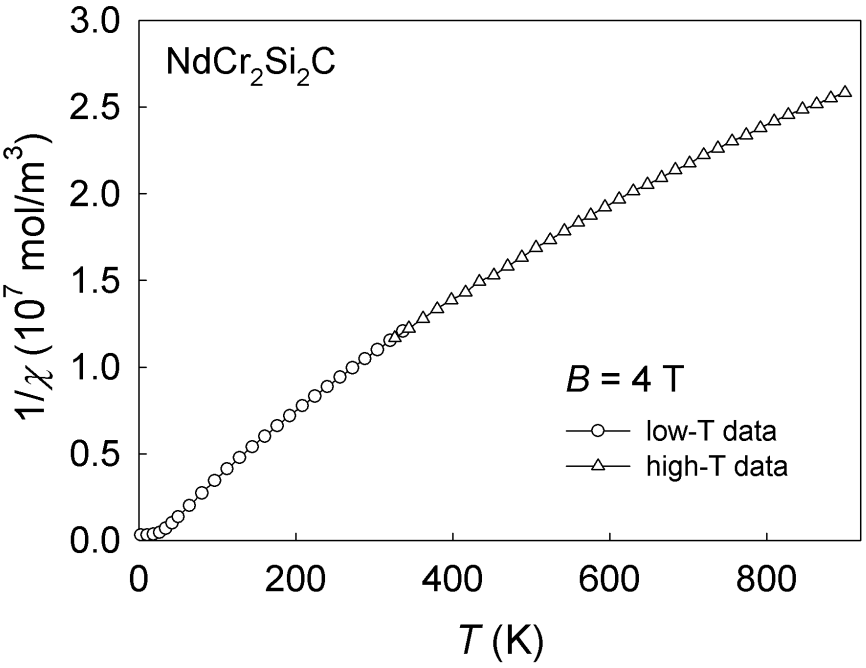

Fig. 5.34: Temperature dependence of the inverse magnetic susceptibility of $NdCr_2Si_2C$ measured at 4 T.

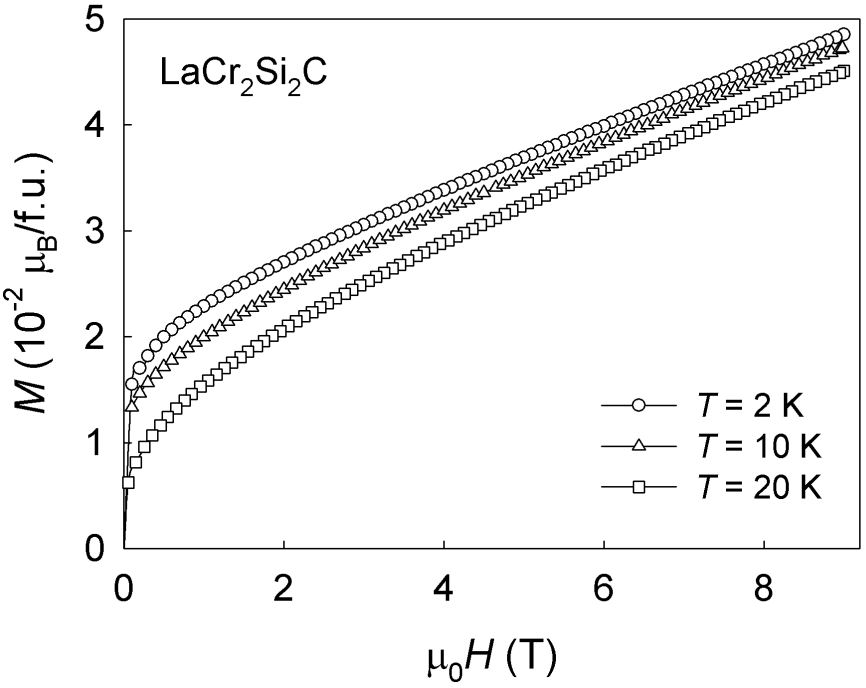

Fig. 5.35: Magnetization isotherms measured on the $LaCr_2Si_2C$ at various temperatures.

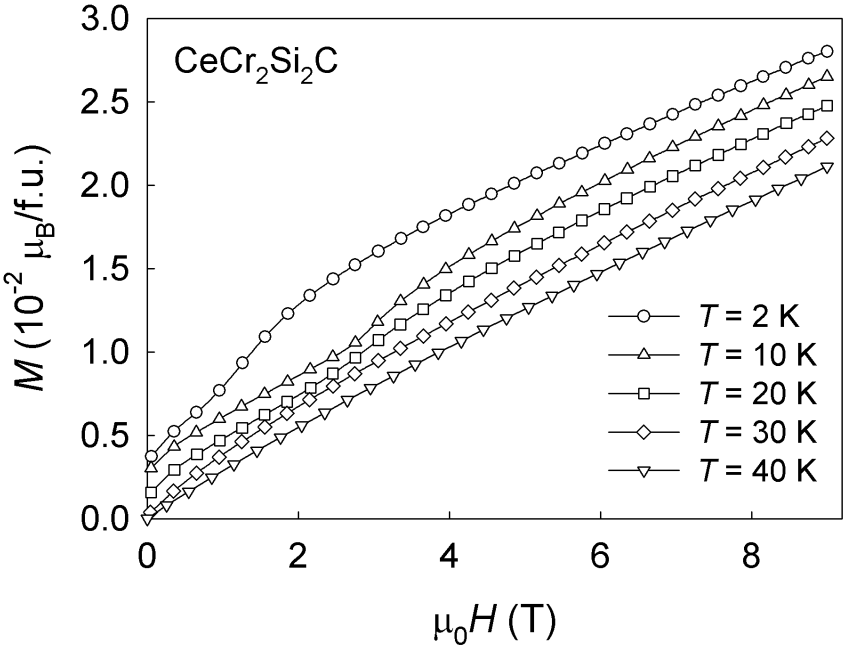

Fig. 5.36: Magnetization isotherms measured on the $CeCr_2Si_2C$ at various temperatures.

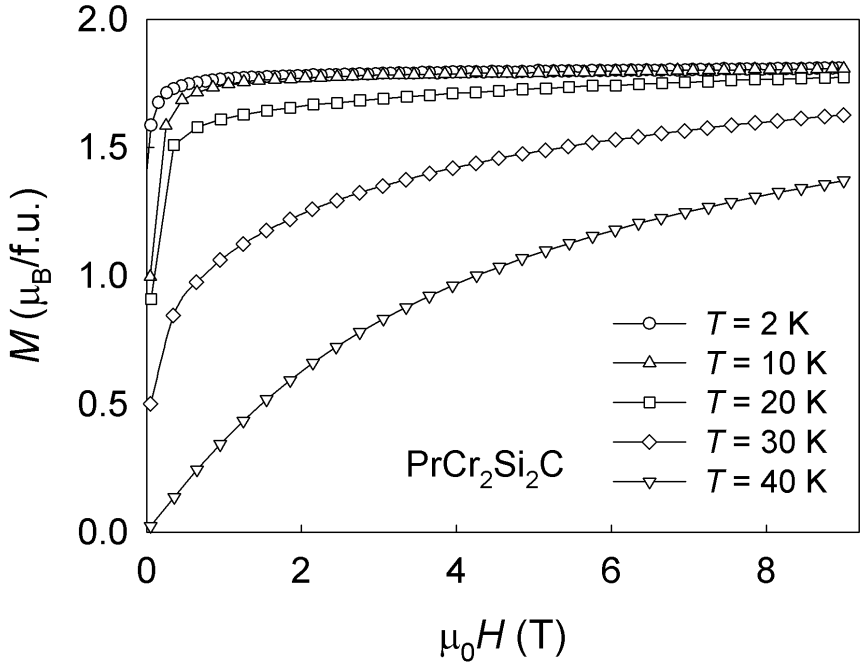

Fig. 5.37: Magnetization isotherms measured on the $PrCr_2Si_2C$ at various temperatures.

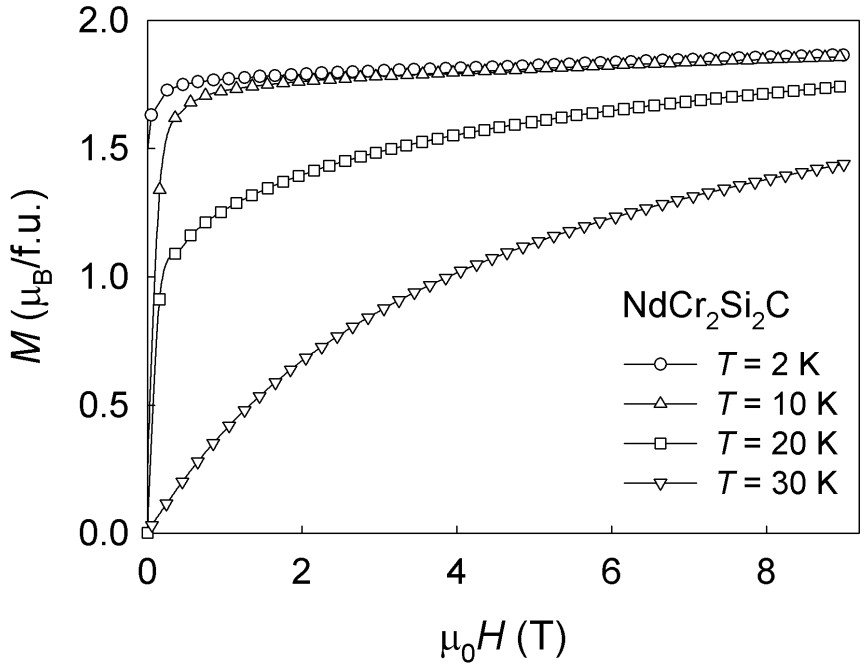

Fig. 5.38: Magnetization isotherms measured on the $NdCr_2Si_2C$ at various temperatures.

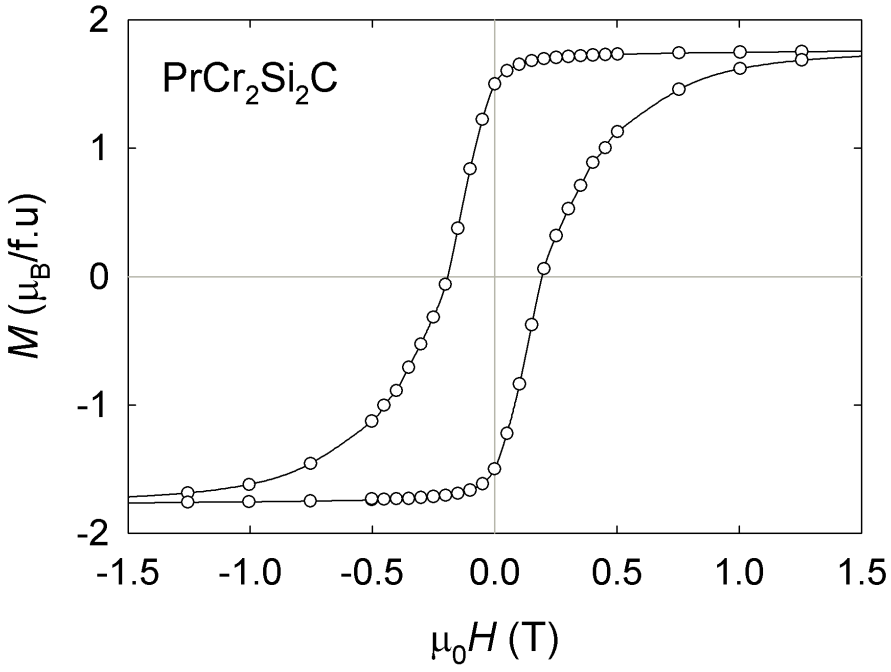

Fig. 5.39: Hysteresis loop of $PrCr_2Si_2C$ at 2 K.

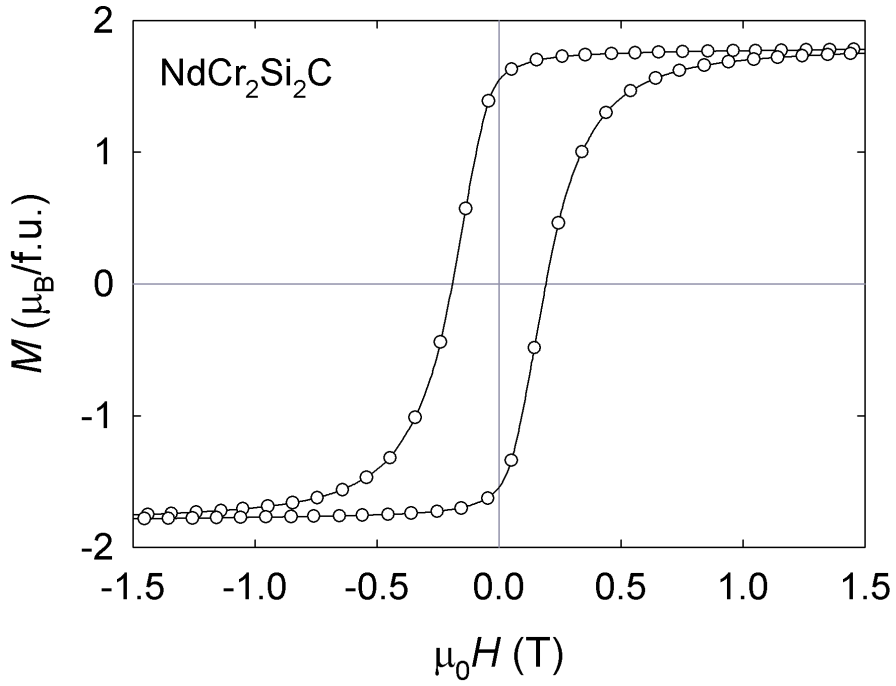

Fig. 5.40: Hysteresis loop of $NdCr_2Si_2C$ at 2 K.

RCr_2Si_2C	H_C (T)	M_r (μ_B/f.u.)	μ_s (μ_B/f.u.)	theor. μ_s for free R^{3+} ion
$PrCr_2Si_2C$	0.25	1.50	1.80	3.20
$NdCr_2Si_2C$	0.19	1.55	1.86	3.27

Table 5.5: The values of coercivity, remanence and saturation moment for $PrCr_2Si_2C$ and $NdCr_2Si_2C$ compounds at 2 K.

magnetic moment along the easy-magnetization axis is about $3.6\mu_B$/f.u., which is considerably larger than the saturation moment of free Pr^{3+} and Nd^{3+} ions, respectively. Therefore, additional contribution, likely arising from the Cr sublattice, is present.

Magnetization measurements of $CeCr_2Si_2C$ single crystal

For $CeCr_2Si_2C$ single crystal, we performed the measurement of both the temperature and field dependence of the magnetization along the *a*- and *c*-axis.

The temperature dependence of the magnetization along the *a*- and *c*-axis is presented in Fig. 5.41. The shape of the 2 T curve indicates the antiferromagnetic behavior below ~ 26 K.

It is evident that there is only a small difference between the measured data along the *a*- and *c*-axis. It could be caused by the low quality of the single crystal or by the fact, that the $CeCr_2Si_2C$ compound is almost isotropic.

The results of the high-temperature magnetization measurement indicate that there is no magnetic ordering of the Cr sublattice up to 900 K.

On the basis of the measurement of magnetization in the temperature range 2–900 K, we plotted the temperature dependence of the inverse magnetic susceptibility (Fig. 5.43). The strong deviation from the Curie-Weiss behavior is observed along both crystallographic axes.

The results of the measurement of the $M(H)$ dependence at various temperatures are presented in Fig. 5.44. At 2 K, the saturation moment is about $0.006\mu_B$/f.u.. As was mentioned above, at 2 K, there is a broad metamagnetic anomaly, which is around 1 T in this measurement, and is shifted to about 3 T at 10 and 20 K, respectively.

Magnetization measurements of $PrCr_2Si_2C$ single crystal

For $PrCr_2Si_2C$ single crystal, both the temperature and field dependence of the magnetization was measured along the *a*- and *c*-axis.

As we assumed, the $PrCr_2Si_2C$ single crystal exhibits strong magnetocrystalline anisotropy. Fig. 5.45 shows the temperature dependence of the magnetization along the *a*- and *c*-axis. We can see, that the magnetization measured along the *c*-axis is nearly five-times larger than the magnetization measured along the *a*-axis. Therefore, the *c*-axis is the easy-magnetization axis for $PrCr_2Si_2C$.

As for the high-temperature magnetization measurement, the situation is similar to the rest of the studied compounds – no anomalies were found to indicate the possible high-temperature ordering of the Cr sublattice.

The plot of the inverse magnetic susceptibility measured along the both crystallographic directions (Fig. 5.48) confirms our assumption, that the *c*-axis is the easy-magnetization axis of $PrCr_2Si_2C$ compound. The $1/\chi$ curves shows a deviation from the Curie-Weiss behavior, therefore the Curie-Weiss law was not finally

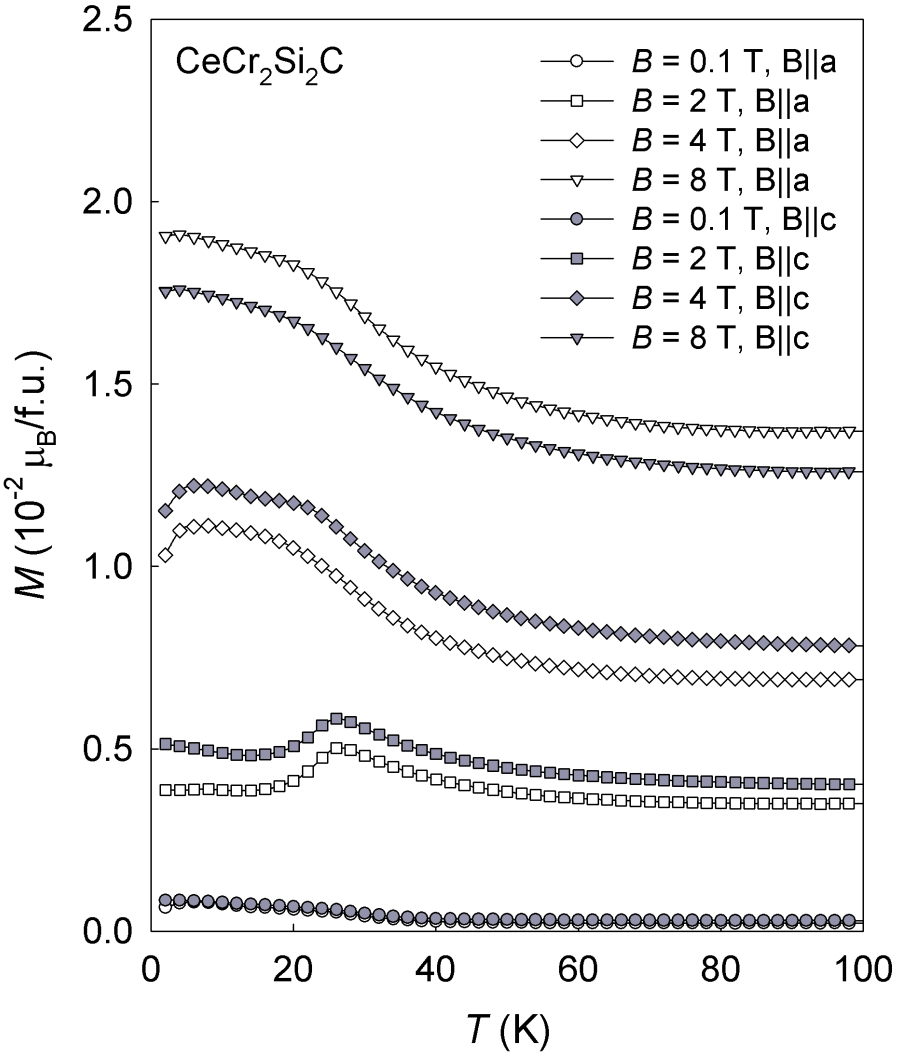

Fig. 5.41: Temperature dependence of the magnetization measured on $CeCr_2Si_2C$ single crystal along the a- and c-axis.

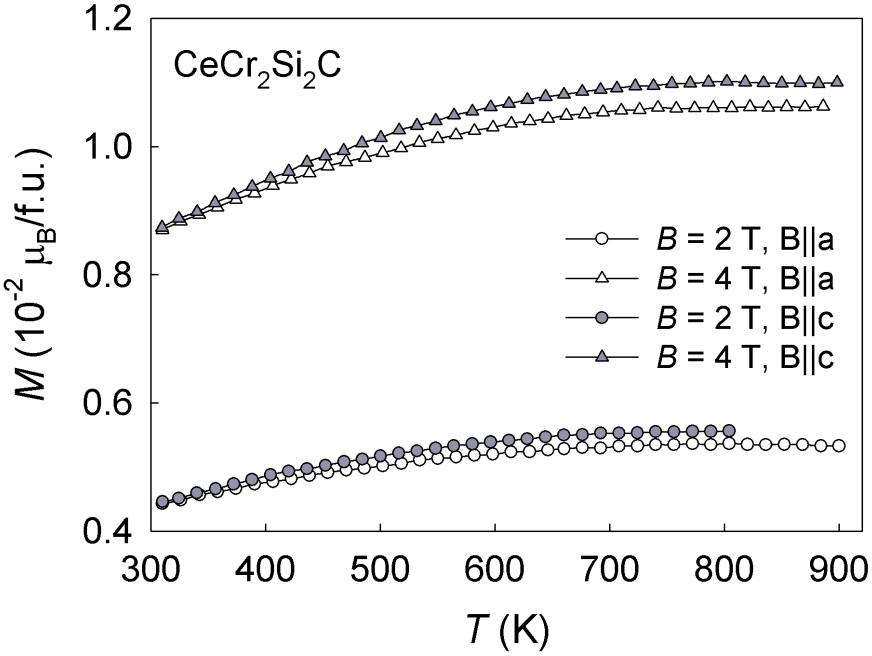

Fig. 5.42: The high-temperature dependence of the magnetization measured on $CeCr_2Si_2C$ single crystal along the a- and c-axis.

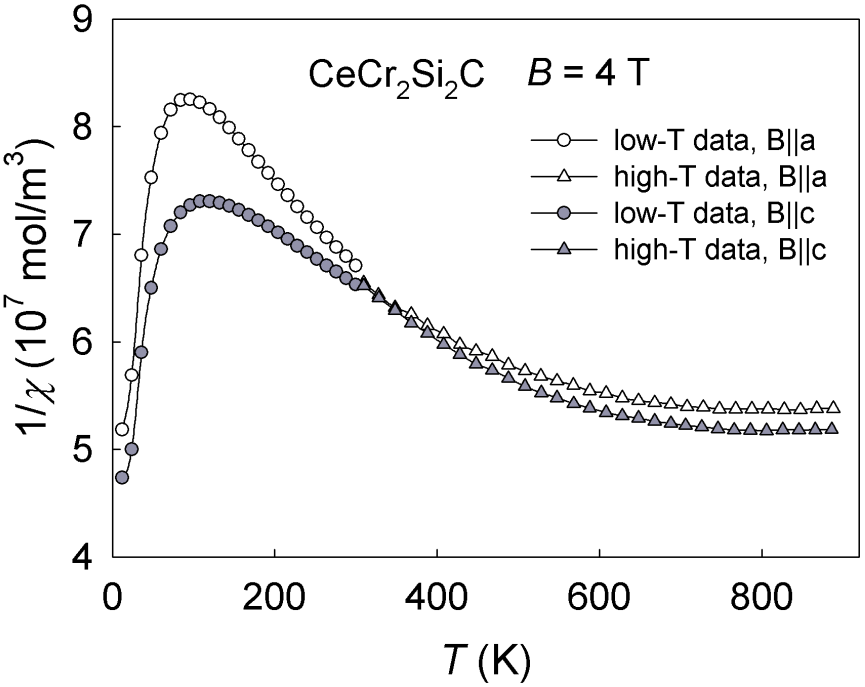

Fig. 5.43: The plot of the inverse magnetic susceptibility measured on $CeCr_2Si_2C$ single crystal along the a- and c-axis measured in the magnetic field $B = 4\,\mathrm{T}$.

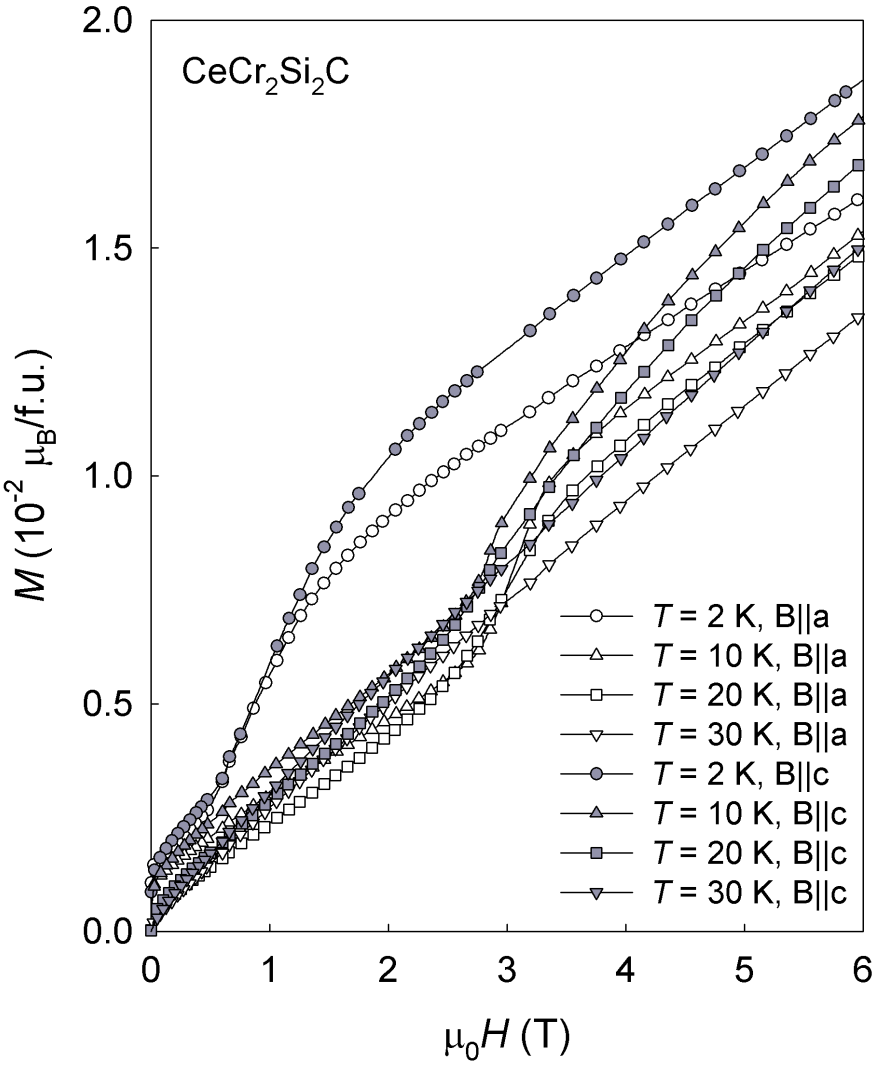

Fig. 5.44: Magnetization isotherms measured on $CeCr_2Si_2C$ single crystal along the a- and c-axis.

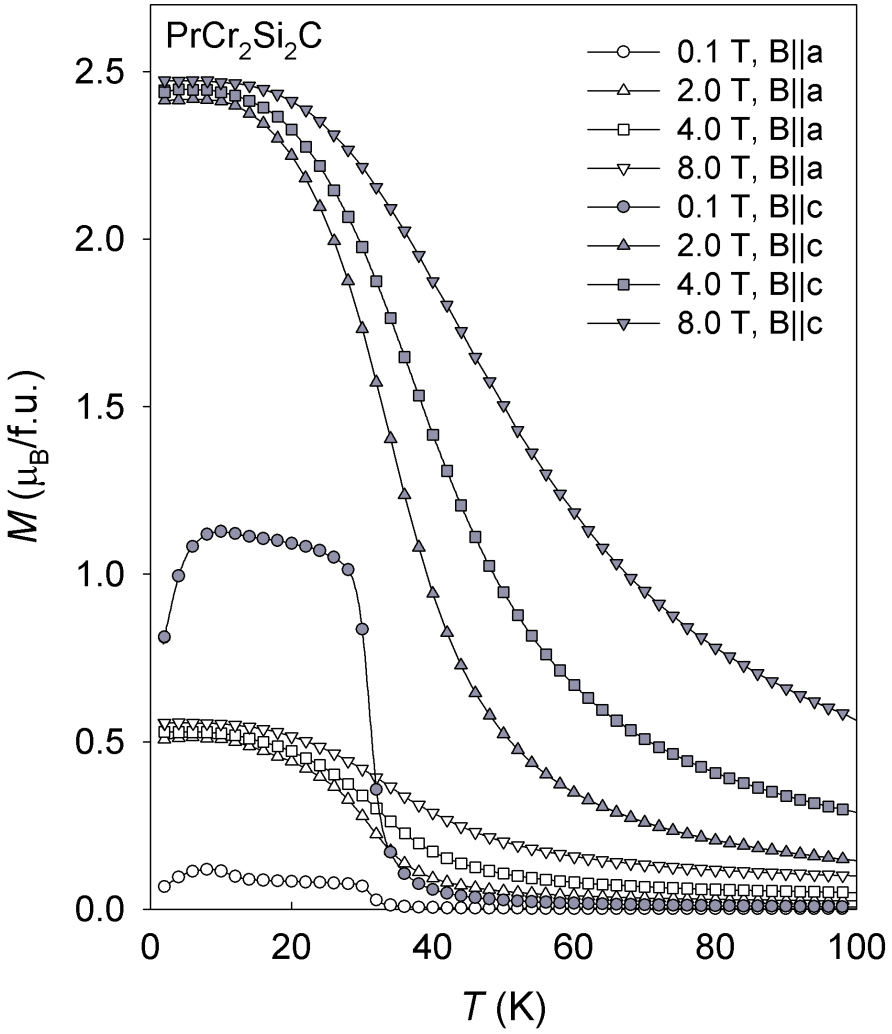

Fig. 5.45: Temperature dependence of the magnetization measured on $PrCr_2Si_2C$ single crystal along the a- and c-axis.

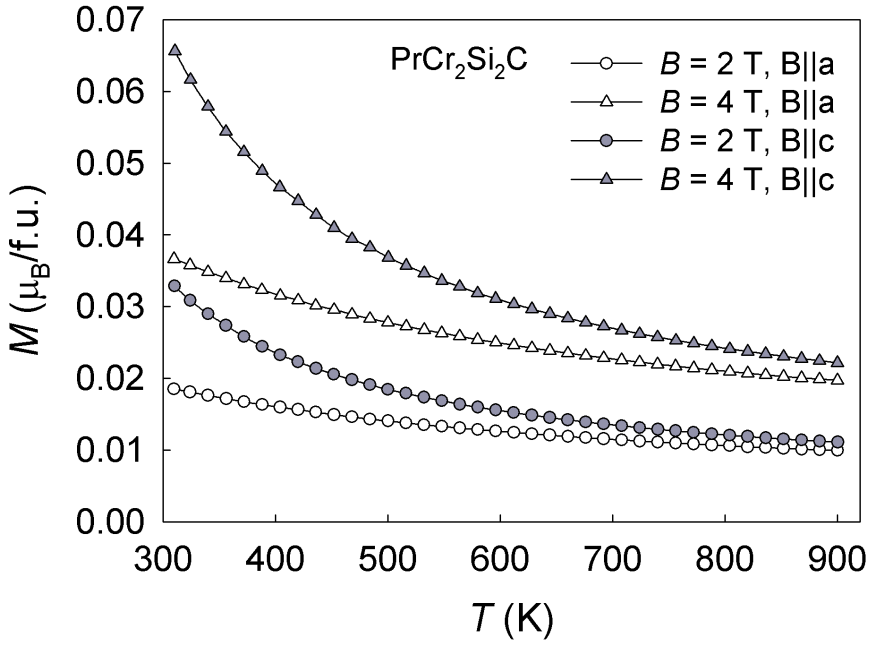

Fig. 5.46: The high-temperature dependence of the magnetization measured on $PrCr_2Si_2C$ single crystal along the a- and c-axis.

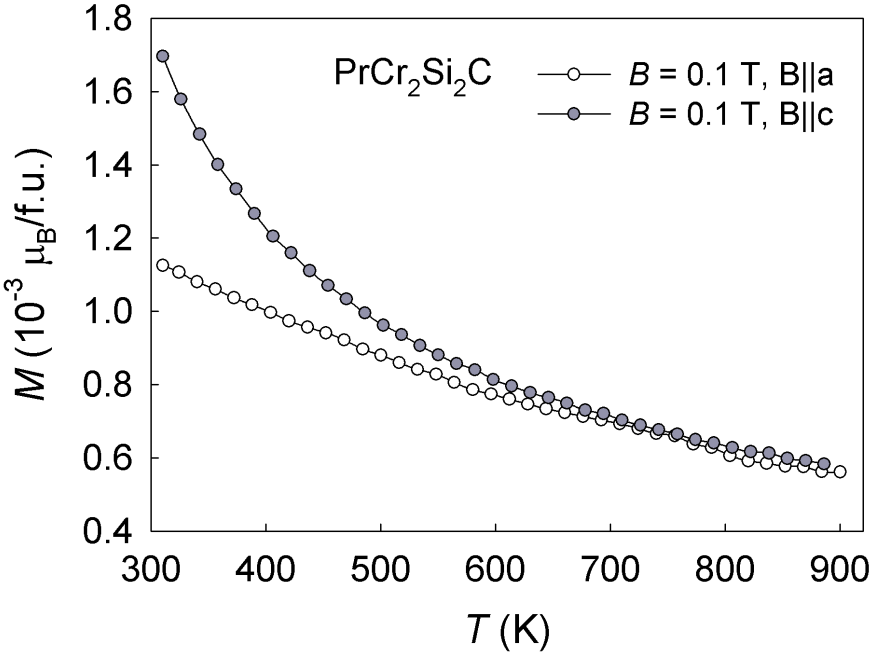

Fig. 5.47: The high-temperature dependence of the magnetization measured on $PrCr_2Si_2C$ single crystal in the magnetic field $B = 0.1\,\mathrm{T}$.

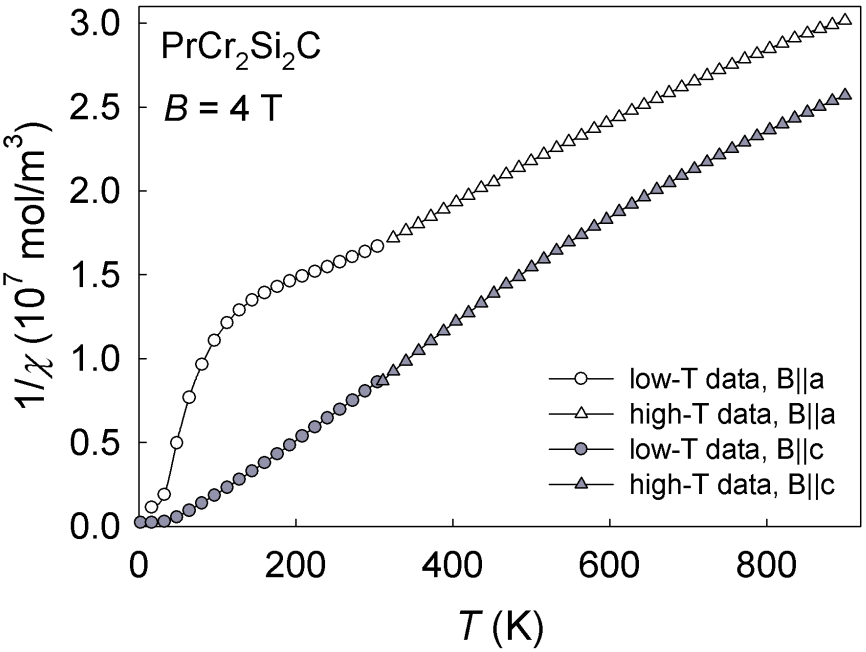

Fig. 5.48: The plot of the inverse magnetic susceptibility measured on $PrCr_2Si_2C$ single crystal along the a- and c-axis in the magnetic field $B = 4\,\mathrm{T}$.

applied. The anisotropic magnetic susceptibility could be described by a sophisticated procedure involving fit of the crystal field term to the experimental data as described in the section 2.1.6.

The strong magnetocrystalline anisotropy is also evident from the measurement of the $M(H)$ curves measured at various temperatures (Fig. 5.49). The obtained values of coercivity, remanence and saturation moment at 2 K are presented in Table 5.6.

$PrCr_2Si_2C$	H_C (T)	M_r (μ_B/f.u.)	μ_s (μ_B/f.u.)
$B \parallel a$	0.30	0.35	0.55
$B \parallel c$	0.15	2.10	2.48

Table 5.6: The values of coercivity, remanence and saturation moment for $PrCr_2Si_2C$ single crystal at 2 K.

The saturated magnetic moment at 2 K is about $2.5\mu_B$/f.u. along the c-axis, and $0.5\mu_B$/f.u. along the a-axis, respectively. The values suggest the following scenario of magnetic ordering in the compound. The Pr magnetic moments are aligned along the c-axis, and they are particularly compensated by the Cr moments order antiparallel along the c-axis. When the field is applied along the a-axis, the Cr spins are rapidly reoriented to the field direction and the sublattice magnetization is saturated, as it is not fixed by the orbital contribution.

The $PrCr_2Si_2C$ can be viewed as a ferrimagnet with the two sublattices, the former with a strong magnetocrystalline anisotropy with the c-axis as the easy-magnetization direction, the later with much lower anisotropy, but the same easy axis.

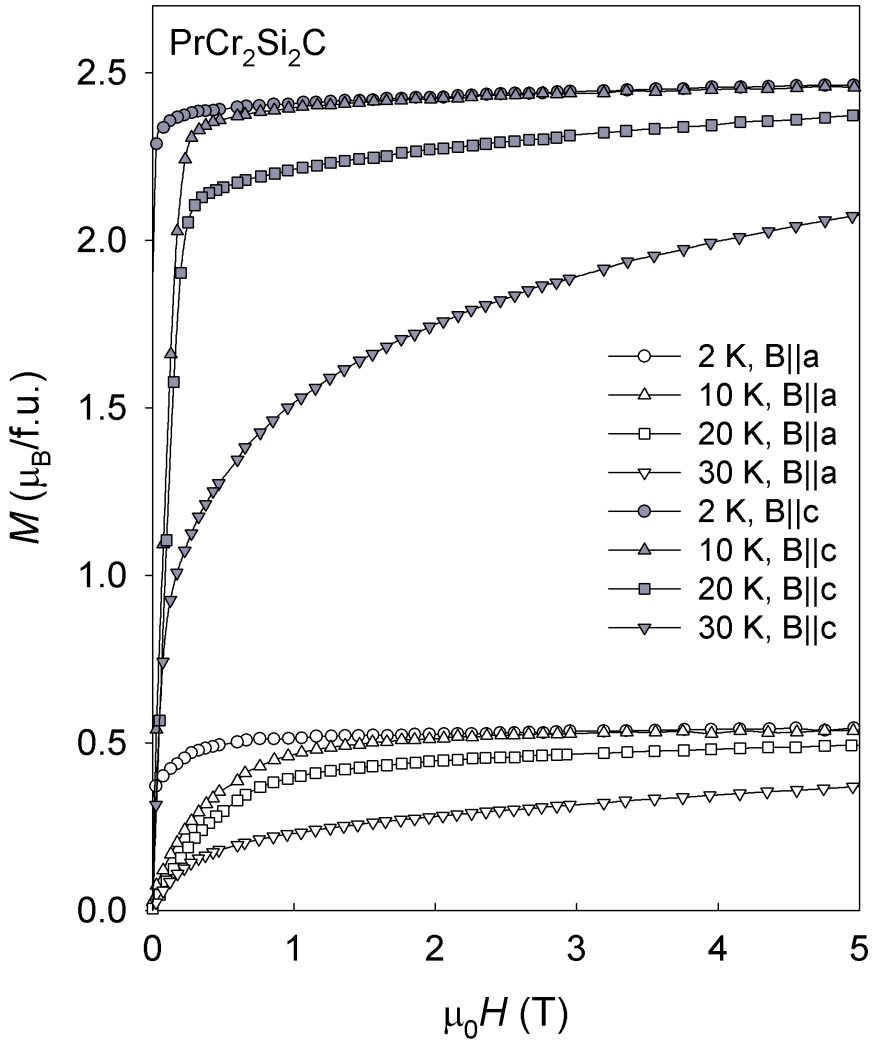

Fig. 5.49: Magnetization isotherms measured on $PrCr_2Si_2C$ single crystal along the a- and c-axis.

5.5 First-principles calculations

The total spin-polarized density of electronic states (DOS) from ferromagnetic LSDA calculations at the experimental equilibrium volume of $LaCr_2Si_2C$ is shown in Fig. 5.50. The chromium $3d$ states form the main contribution to the occupied energy range from -5 eV to the Fermi level and a clear exchange shift is visible

between the spin-up states and the spin-down states. The calculated stable spin magnetic moment of Cr is about $0.5\mu_B$. The precise value depends on the method used (LSDA or GGA). The unoccupied $4f$ states are more than 3 eV above the Fermi level (the pronounced spin-up and spin-down peaks). The electronic structure of $PrCr_2Si_2C$ is very similar to Fig. 5.50 with the $4f$ states localized below Fermi level. The itinerant magnetic moment of chromium is larger ($0.7\mu_B$) since the moment is now stabilized by the $5d$ states of Pr which are polarized by the localized Pr spin moment of about $2\mu_B$ and strongly hybridized with the Cr $3d$ states. This antiferromagnetic $5d$-$3d$ spin polarization further increases the Cr spin moment in comparison to $LaCr_2Si_2C$.

5.6 Results summary

The most important results of our investigations are summarized in this section.

- We investigated possibilities of formation of the $PrCr_2Si_2$ phase. The unsuccessful synthesis of this compound confirmed the fact, that the RCr_2Si_2 phases are not stable for the light rare earths.

- On the basis of the AC-susceptibility measurement, we determined the Néel temperature for the $TbCr_2Si_2$ and $ErCr_2Si_2$ compounds as 3 and 2 K, respectively. Closer inspection of the $M(H)$ dependence revealed a metamagnetic transition into a field-induced ferromagnetic state in $TbCr_2Si_2$, and a saturation already at 2 T in $ErCr_2Si_2$. The obtained values of the effective moment are 10.1 and $9.8\mu_B$/f.u. for $TbCr_2Si_2$ and $ErCr_2Si_2$, respectively.

- For $LaCr_2Si_2C$ and $CeCr_2Si_2C$, the results of the specific-heat measurement show an additional contribution below 20 K, which may be related to the magnetic behavior of the Cr sublattice. It is also supported by the magnetization and AC-susceptibility measurements.

- We observe the ferromagnetic ordering of the rare-earth sublattice below the Curie temperature of 30 and 21 K for $PrCr_2Si_2C$ and $NdCr_2Si_2C$, respectively. Both compounds show a strong ferromagnetic component and rapid saturation in the $M(H)$ dependence. For $PrCr_2Si_2C$, the low-temperature inverse magnetic susceptibility follows a Curie-Weiss law with an effective magnetic moment $\mu_{\text{eff}} = (4.0\pm0.1)\mu_B$/f.u. and a paramagnetic Curie temperature $\theta_p = (33 \pm 5)$ K. The obtained value of the effective moment suggests an additional contribution by the Cr sublattice.

- The results of the magnetization measurements on the $CeCr_2Si_2C$ single crystal suggest a possible metamagnetic transition around 1 T at 2 K. There is only small difference between the measured data along the a- and c-axis, probably caused by the low quality of the single crystal.

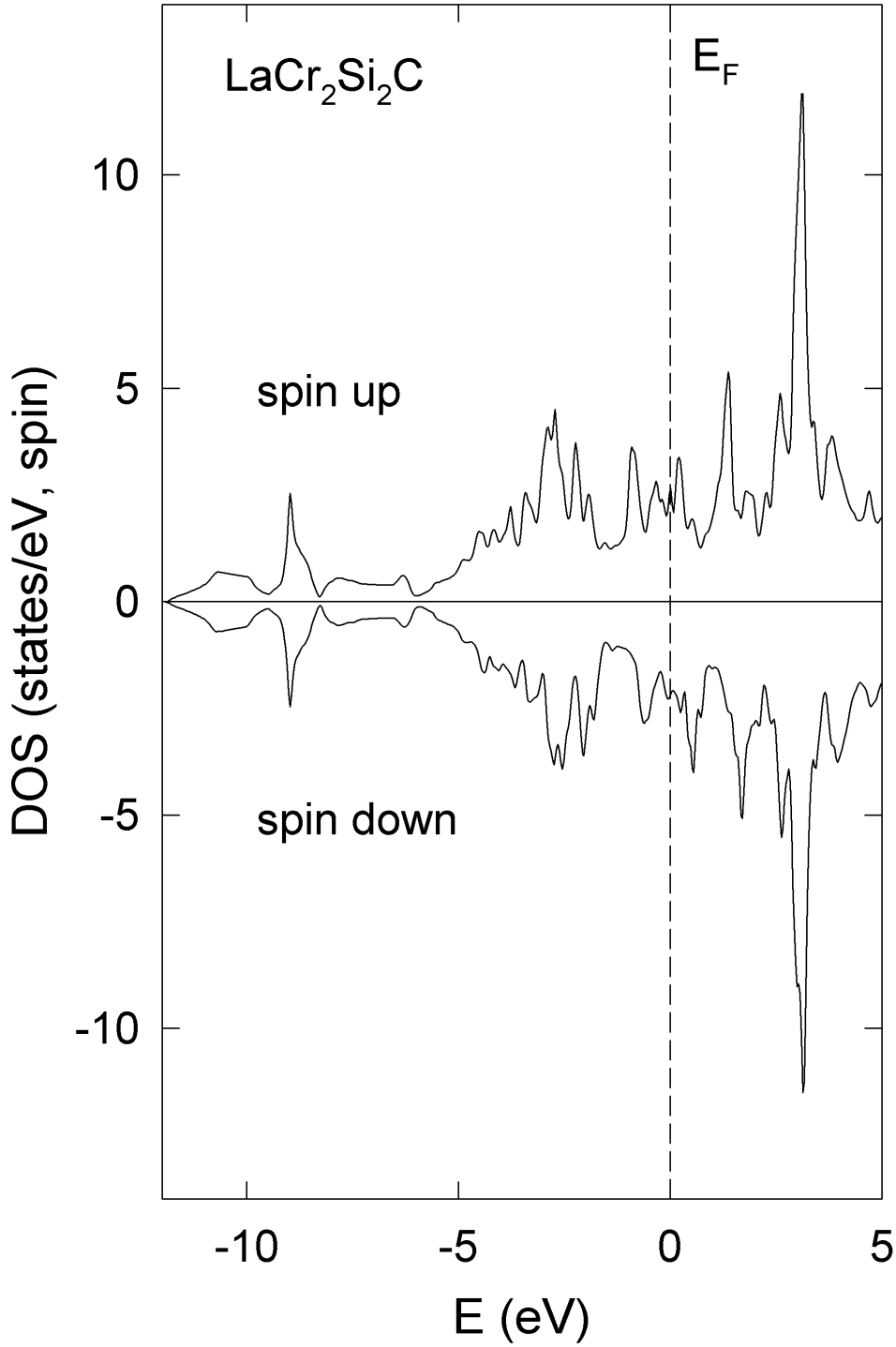

Fig. 5.50: Spin-polarized DFT-calculated DOS of $LaCr_2Si_2C$. Positive numbers mean spin-up DOS and negative numbers mean spin-down DOS. The Fermi level is set to zero energy.

- The magnetization and AC-susceptibility measurements performed for the $PrCr_2Si_2C$ single crystal confirmed our expectation of the strong magnetocrystalline anisotropy. The results indicate, that the c-axis is the easy-magnetization axis.
- The detailed first-principles calculations were performed for the $LaCr_2Si_2C$ and $PrCr_2Si_2C$ compounds obtaining the calculated stable itinerant magnetic moment of Cr of about 0.5 and $0.7\mu_B$, respectively.

Chapter 6

Conclusions

We have prepared the polycrystalline samples of RCr_2Si_2 (R = Pr, Tb, Er) and RCr_2Si_2C (R = La, Ce, Pr, Nd) compositions and single crystals of $CeCr_2Si_2C$ and $PrCr_2Si_2C$. The samples were prepared from the rare-earth metals purified by the solid-state electrotransport in order to obtain as high purity as possible. All samples were characterized by XRD and found to be single-phased except the $PrCr_2Si_2$, which was not further investigated.

The RCr_2Si_2 and RCr_2Si_2C compounds were found to be isostructurally crystallizing in the tetragonal structure of the $ThCr_2Si_2$- and the $CeMg_2Si_2$-type, respectively. For $TbCr_2Si_2$, $ErCr_2Si_2$ and $CeCr_2Si_2C$ compounds, the lattice parameters obtained on the basis of the Rietveld analysis are in a good agreement with the previous results [15, 18].

All studied samples were further investigated by specific-heat, magnetization and AC-susceptibility measurements in the wide temperature range 2–900 K and in magnetic fields up to 9 T. The rare-earth sublattice in the RCr_2Si_2 compounds orders magnetically in low temperatures at about 2 K, whilst no high-temperature ordering of the Cr sublattice was observed.

The measurements performed for the RCr_2Si_2C compounds indicate that the Cr sublattice orders magnetically. This is supported by the first-principles DFT calculations for R = La, Pr. The calculated stable itinerant magnetic moment of Cr is about 0.5 and $0.7\mu_B$ for La and Pr, respectively. However, the high-temperature magnetization measurements show no anomaly, which could be an indicative of the possible magnetic ordering of the Cr sublattice already at high temperatures.

In $PrCr_2Si_2C$ and $NdCr_2Si_2C$, also the rare-earth sublattice orders ferromagnetically with the Curie temperature of 30 and 21 K for $PrCr_2Si_2C$ and $NdCr_2Si_2C$, respectively.

The magnetization measurements performed on the $PrCr_2Si_2C$ single crystal confirmed the presence of the strong magnetocrystalline anisotropy, as expected for this type of compounds.

The results obtained on the novel intermetallic compounds stimulated our interest in continuous investigation of magnetism of those $ThCr_2Si_2$-type related

compounds.

We already planned a powder neutron diffraction experiment in order to determine magnetic structures of the RCr_2Si_2 (R = Tb, Er) and RCr_2Si_2C (R = La, Ce, Pr, Nd) compounds. Further experiments on single crystals are in progress in order to get a better insight into magnetic ordering and magnetocrystalline anisotropy of the compounds.

After succeeding in crystal-growth of some of the compounds, we would like to treat the crystals by additional annealing and by solid-state electrotransport, respectively, to get excellent quality of the material for investigations of transport properties, low-temperature phenomena in the Cr sublattice, and potentially de Haas van Alphen effect. The knowledge of the electronic structure and the Fermi surface of the compounds would help to explain unusual phenomena observed on the macroscopic physical properties.

References

[1] Kittel, Ch.: Úvod do fyziky pevných látek, Academia, Praha, (1985).

[2] Stevens, K. W. H.: Proc. Phys. Soc. A **65** (1952) 209.

[3] Ashcroft, N. W., Mermin, N. D.: Solid State Physics, Thomson Learning, Inc., (1976).

[4] Ruderman, M. A., Kittel, C.: Phys. Rev. **96** (1954) 99.

[5] Martin, C. A.:J. Phys. Cond. Mater. **3** (1991), 5967.

[6] Jordan, R. G.: Contemp. Phys. **15** (1974), 375-400.

[7] Rietveld, H. M.: J. Appl. Crystallogr. **2** (1969), 65.

[8] Rodriguez-Carvajal, J.: Physica B **192** (1993) 5.

[9] Valvoda, V.: Rentgenová strukturní analýza, SPN, skriptum MFF UK, (1982).

[10] PPMS - Physical Property Measurement System, User's Manual, Quantum Design, San Diego, (2004).

[11] MPMS - Magnetic Property Measurement System, User's Manual, Quantum Design, San Diego, (2004).

[12] Perdew, J. P., Wang, Y.: Phys. Rev. B **45** (1992),13244.

[13] Perdew, J. P., Burke, K., Ernzerhof, M.: Phys. Rev. Lett. **77** (1996), 3865.

[14] Blaha, P., Schwarz, K., Madsen, G., Kvasnicka, D., Luitz, J.: WIEN2k, TU Wien, Austria, (2001), ISBN: 3-9501031-1-2.

[15] Dommann, A., Hulliger, F., Baerlocher, Ch.: J. Less-Common Met. **138** (1988) 113-121.

[16] Dirken, M. W., Thiel, R. C., Buschow, K. H. J.: J. Less-Common Met. **147** (1989) 91.

[17] Prots, Y. M., Salamakha, P. S., Sologub, O. L., Bodak, O. I.: J. Alloys Compd. **215** (1994) 235.

[18] Moze, O., Hofmann, M., Cadogan, J. M., Buschow, K. H. J., Ryan, D. H.: Eur. Phys. J. B **36** (2003) 511-518.

[19] Szytula, A.: Handbook of Magnetic Materials, vol. 6, Elsevier, Amsterdam, (1991) pp.87-179.

[20] Hofmann, M., Campbell, S. J., Kennedy, S. J., Zhao, X. L.: J. Magm. Magn. Mater. **176** (1997) 279.

[21] Pinto, H., Shaked, H.: Phys. Rev. B **7** (1973) 3261.

[22] Moze, O., Hofmann, M., Buschow, K. H. J.: J. Alloys Compd. **308** (2000) 60-63.

[23] Tang, Ch., Fan, S., Zhu, M.: J. Alloys Compd. **299** (2000) 1-4.

[24] Moon, R. M., Koehler, W. C., Child, H. R., Raubenheimer, L. J.:Phys. Rev. **176** (1968) 722-731.

[25] Mihalik, M., Vejpravova, J., Rusz, J., Divis, M., Svoboda, P., Sechovsky, V., Mihalik, M.: Phys. Rev. B **70** (2004) 134405.